(12) INTERNATIONAL APPLICATION PUBLISHED UNDER THE PATENT COOPERATION TREATY (PCT)

(19) World Intellectual Property Organization
International Bureau

(43) International Publication Date
08 October 2020 (08.10.2020)

WIPO | PCT

(10) International Publication Number
WO 2020/206365 A1

(51) International Patent Classification:
H01M 10/0565 (2010.01) *H01M 10/052* (2010.01)

(21) International Application Number:
PCT/US2020/026737

(22) International Filing Date:
03 April 2020 (03.04.2020)

(25) Filing Language: English

(26) Publication Language: English

(30) Priority Data:
62/830,217 05 April 2019 (05.04.2019) US

(71) Applicant: **THE BOARD OF TRUSTEES OF THE LELAND STANFORD JUNIOR UNIVERSITY** [US/US]; Office of the General Counsel, Building 170, Third Floor, Main Quad, P.O. Box 20386, Stanford, California 94305-2038 (US).

(72) Inventors: **CUI, Yi**; Office of the General Counsel, Building 170, Third Floor, Main Quad, P.O. Box 20386, Stanford, California 94305 (US). **WAN, Jiayu**; Office of the General Counsel, Building 170, Third Floor, Main Quad, P.O. Box 20386, Stanford, California 94305 (US). **XIE, Jin**; Office of the General Counsel, Building 170, Third Floor, Main Quad, P.O. Box 20386, Stanford, California 94305 (US).

(74) Agent: **SHELTON, Daniel R.** et al.; Foley & Lardner LLP, 3000 K Street N.W., Suite 600, Washington, District of Columbia 20007-5109 (US).

(81) Designated States *(unless otherwise indicated, for every kind of national protection available)*: AE, AG, AL, AM, AO, AT, AU, AZ, BA, BB, BG, BH, BN, BR, BW, BY, BZ, CA, CH, CL, CN, CO, CR, CU, CZ, DE, DJ, DK, DM, DO, DZ, EC, EE, EG, ES, FI, GB, GD, GE, GH, GM, GT, HN, HR, HU, ID, IL, IN, IR, IS, JO, JP, KE, KG, KH, KN, KP, KR, KW, KZ, LA, LC, LK, LR, LS, LU, LY, MA, MD, ME, MG, MK, MN, MW, MX, MY, MZ, NA, NG, NI, NO, NZ, OM, PA, PE, PG, PH, PL, PT, QA, RO, RS, RU, RW, SA, SC, SD, SE, SG, SK, SL, ST, SV, SY, TH, TJ, TM, TN, TR, TT, TZ, UA, UG, US, UZ, VC, VN, WS, ZA, ZM, ZW.

(84) Designated States *(unless otherwise indicated, for every kind of regional protection available)*: ARIPO (BW, GH, GM, KE, LR, LS, MW, MZ, NA, RW, SD, SL, ST, SZ, TZ, UG, ZM, ZW), Eurasian (AM, AZ, BY, KG, KZ, RU, TJ,

(54) Title: ULTRATHIN, FLEXIBLE, SOLID POLYMER COMPOSITE ELECTROLYTE WITH ALIGNED NANOPOROUS HOST FOR LITHIUM BATTERIES

FIGURE 1

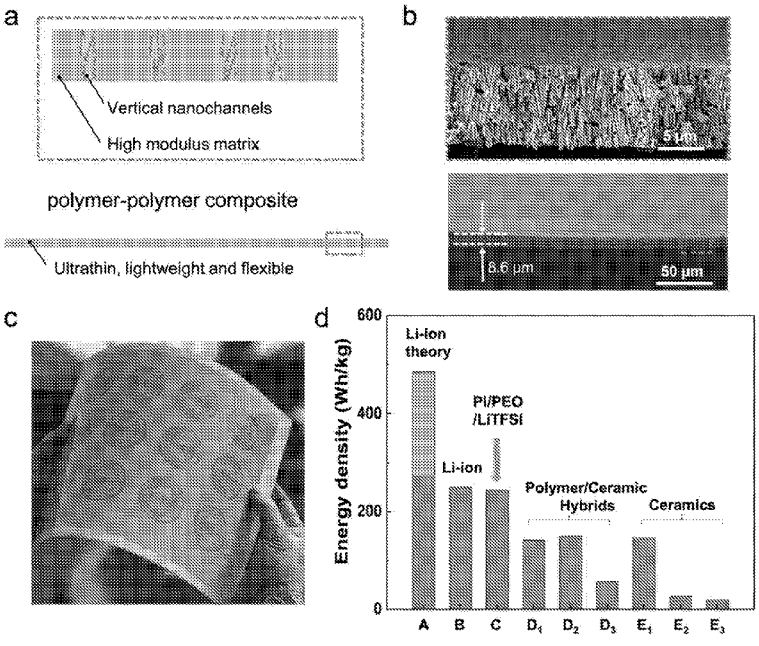

(57) Abstract: This disclosure provides novel composite solid electrolytes, batteries containing these electrolytes and methods of manufacturing the electrolytes and batteries. Some embodiments include a composite solid electrolyte, comprising: a porous matrix having channels; and ionically conducting fillers disposed within the channels. In some embodiments, the porous matrix is a porous polymeric matrix.

[Continued on next page]

WO 2020/206365 A1

TM), European (AL, AT, BE, BG, CH, CY, CZ, DE, DK, EE, ES, FI, FR, GB, GR, HR, HU, IE, IS, IT, LT, LU, LV, MC, MK, MT, NL, NO, PL, PT, RO, RS, SE, SI, SK, SM, TR), OAPI (BF, BJ, CF, CG, CI, CM, GA, GN, GQ, GW, KM, ML, MR, NE, SN, TD, TG).

Declarations under Rule 4.17:

— *as to applicant's entitlement to apply for and be granted a patent (Rule 4.17(ii))*

— *as to the applicant's entitlement to claim the priority of the earlier application (Rule 4.17(iii))*

Published:

— *with international search report (Art. 21(3))*

Ultrathin, Flexible, Solid Polymer Composite Electrolyte with Aligned Nanoporous Host for Lithium Batteries

Cross-reference to related applications

[0001] This application claims the benefit of U.S. Provisional Patent Application No. 62/830,217, filed April 5, 2019, which is incorporated by reference herein in its entirety.

Statement Regarding Federally Sponsored Research or Development

[0002] This invention was made with government support awarded by the Assistant Secretary for Energy Efficiency and Renewable Energy, Office of Vehicle Technologies of the US Department of Energy under the Battery Materials Research (BMR) program and Battery 500 Consortium program. The government may have certain rights in the invention.

Background

[0003] Li-ion batteries (LIBs) are the dominant energy storage device. In pursuit of LIBs with better performance, tremendous progress has been made on various components in batteries. However, the dilemma of high performance versus safety of LIBs remains a challenge, leading to catastrophic battery incidents. The ever-increasing demand for high energy density LIBs urges the utilization of the ultimate metallic Li anode, which further complicates safety issues. Li dendrites formed during electrochemical Li plating and stripping can penetrate the separator, leading to battery short circuiting, and eventually fire and tragedies.

[0004] To address the aforementioned safety concerns, solid-state electrolytes (SSE) have attracted great attention as replacements for the flammable liquid electrolyte in LIBs. Ideally, SSEs should be highly ionically conductive, mechanically strong, nonvolatile, nonflammable, and chemically/electrochemically stable within the battery operation window. Different types of SSE materials are proposed for safer LIBs. These SSEs can be summarized in three categories: inorganic (ceramic/glass) solid electrolytes, solid polymer electrolytes (SPEs), and their hybrids. Inorganic SSEs generally have the highest ionic conductivity among all types of SSEs, with some (sulfide superionic conductors) even exceeding that of liquid electrolytes. However, the brittle nature of inorganic SSE pellets may greatly hinder their processability and use in practical applications such as in electrical vehicles, where even a

small bump may cause structural failure. Inorganic SSEs are also not flexible and are relatively thick (> about 200 μm) in order to preserve their intact structure during handling. An intrinsic high electronic conductivity in certain inorganic SSEs, especially at grain boundaries, can lead to hazardous direct Li deposition inside of them. The above issues therefore should be addressed before utilizing inorganic SSEs in all-solid-state batteries

[0005] SPEs are mainly composed of uniform mixtures of solid polymers and Li salts. These SSEs are proposed due to their high flexibility, lightweight, low cost and ready scalability. However, the intrinsic softness of these polymer systems and their moderate ionic conductivity hinder the use of pure polymer/Li salt composites in LIBs. In the case of polyethylene oxide (PEO), adding plasticizers or grafting functional branches to PEO chains can enhance the ionic conductivity and modulus of the SPE. Even so, PEO itself is still flammable, making its SPEs similarly unfavorable compared to liquid electrolytes. The combination of organic and inorganic solid electrolytes into a composite solid electrolyte is promising because it improves ionic conductivity without sacrificing the flexibility of the polymer electrolyte. The enhanced ionic conductivity arising from aligned composite polymer-inorganic SPE structures furthers the advantages of these SSEs. Aligning Li conducting ceramic nanowires in a horizontal configuration can improve ionic conductivity in polyacrylonitrile (PAN)/$LiClO_4$ polymer electrolyte systems. Nevertheless, even with such SSE systems, it is difficult to create highly ionic conductive (> about 10^{-4} S/cm), thin SSEs (< about 10 μm) at room temperature by positioning inorganic components in a vertical configuration, while simultaneously obtaining stable cycling performance within a full battery.

[0006] It is against this background that a need arose to develop the embodiments described in this disclosure.

Summary

[0007] This disclosure provides novel composite solid electrolytes, batteries containing these electrolytes and methods of manufacturing the electrolytes and batteries.

[0008] Some embodiments include a composite solid electrolyte, comprising: a porous matrix having channels; and ionically conducting fillers disposed within the channels. In some embodiments, the porous matrix is a porous polymeric matrix. In some embodiments, the

porous polymeric matrix is a porous polymeric film. In some embodiments, the porous polymeric film has a first major surface and an opposite, second major surface, and the channels extend at least partially through a thickness of the porous polymeric film between the first surface and the second surface. In some embodiments, at least some of the channels extend fully through the thickness of the porous polymeric film between the first surface and the second surface. In some embodiments, an alignment direction is specified as orthogonal to the first surface or the second surface, and at least some of the channels extend between the first surface and the second surface along respective longitudinally extending directions that are within ±35° of the alignment direction. In some embodiments, the thickness of the porous polymeric film is about 100 μm or less. In some embodiments, the porous matrix has an elastic modulus of about 10 MPa or greater. In some embodiments, the channels have lateral dimensions in a range of about 1 nm to about 1000 nm. In some embodiments, the ionically conducting fillers include a solid polymer electrolyte. In some embodiments, the solid polymer electrolyte includes a polymer and a lithium-containing salt.

[0009] Other aspects of the disclosure include a solid-state lithium battery, comprising: a cathode; an anode; and the composite solid electrolyte of any of the embodiments disclosed herein disposed between the cathode and the anode. In some embodiments, the anode is a metallic lithium anode.

[0010] Other aspects of the disclosure include a manufacturing method of a composite solid electrolyte, comprising: providing a porous matrix having channels; infusing a solution of a polymer and a lithium-containing salt into the channels of the porous matrix; and heating the infused porous matrix to form the composite solid electrolyte. In some embodiments, the resulting solid electrolyte is any of the embodiments disclosed herein.

[0011] Both the foregoing summary and the following detailed description are exemplary and explanatory. They are intended to provide further details, but are not to be construed as limiting. Other objects, advantages, and novel features will be readily apparent to those skilled in the art from the following detailed description.

Brief Description of Drawings

[0012] Figure 1 shows a design of polymer-polymer composite all-solid-state electrolyte. Figure 1(a) shows a schematic image showing the design principles of the polymer-polymer

composite all-solid-state electrolyte; Figure 1(b) shows cross-sectional SEM images of an ultrathin nanoporous PI film (bottom) with zoomed in image of the aligned nanopores (top); Figure 1(c) shows a photo image of a large scale porous PI film; Figure 1(d) shows an energy density chart of batteries where different electrolytes, battery casings, separators, liquid/solid electrolytes are all taken into account (D_1-D_3 denote polymer/ceramic composite SSEs, where D_1 and D_2, are LLZO/PEO/LiTFSI composite and D_3 is SiO_2/PEO/$LiClO_4$ composite; E_1-E_3 denote ceramic type SSEs, where E_1 is ultrathin LLZO, E_2 is regular LGPS, and E_3 is regular LLZO, details in Table 1 and Figure 7).

[0013] Figure 2 shows characterization and understanding of PEO/LiTFSI in aligned channels. SEM image (from top view) before Figure 2(a) and after Figure 2(b) PEO/LiTFSI infiltration into the porous PI film; SEM image (from side view) before Figure 2(c) and after Figure 2(d) PEO/LiTFSI infiltration in the porous PI film. Figure 2(e) shows Arrhenius ionic conductivity plots of PEO/LiTFSI thin film solid polymer electrolyte and PEO/LiTFSI within PI/PEO/LiTFSI solid polymer electrolyte. Figure 2(f) shows selected temperature dependent EIS plots of PI/PEO/LiTFSI solid polymer electrolyte. 2D WAXS plots of Figure 2(g) a PEO/LiTFSI thin film and Figure 2(h) PEO/LiTFSI infiltrated in an AAO template with about 200 nm diameter pores. Simulation model of Li^+ transport in Figure 2(i) random system and Figure 2(j) z-aligned PEO system. ($TFSI^-$ ions are not shown in the schematic images) Figure 2(k) shows mean square displacement of Li transport in random and aligned PEO systems at log scale (Inset in the same plot at linear scale).

[0014] Figure 3 shows mechanical property and fire-retarding property of PI/PEO/LiTFSI. Figure 3(a) shows long-term cycling of symmetrical Li-Li cells with PEO/LiTFSI thin film electrolyte and PI/PEO/LiTFSI SPE electrolyte at about 60 °C. Inset is the voltage profile of Li/PI/PEO/LiTFSI/Li at the 200^{th}, 500^{th} and 800^{th} hours, respectively. Each cycle lasts for one hour. Figure 3(b) shows stress-strain curve of porous PI film *vs.* PEO/LiTFSI (EO:Li=about 10:1) film. SEM images showing Li deposition morphology on Cu with Figure 3(c) liquid electrolyte (inset typical zoomed-in SEM image of Figure 3(c)). Figure 3(d) shows PI/PEO/LiTFSI solid electrolyte (inset shows one of the protrusions cut by FIB). Figure 3(e) are photo images of flame test on a regular PP/PE/PP separator, a PEO/LiTFSI film, and a PI film.

[0015] Figure 4 shows full cell performance with PI/PEO/LiTFSI based batteries. Figure 4(a) shows a voltage profile of a Li/PI/PEO/LiTFSI/LFP cell at different charging rates, cycled at about 60 °C. Dashed line is the Li/PEO/LiTFSI/LFP cell at C/10, at about 60 °C. Figure 4(b) shows cycling performance of a Li/PI/PEO/LiTFSI/LFP cell at different charging rates, cycled at about 60 °C. Figure 4(c) shows capacity retention performance of Li/PI/PEO/LiTFSI/LFP and Li/PEO/LiTFSI/LFP cells at C/2, cycled at about 60 °C. Figure 4(d) shows a voltage profile and Figure 4(e) shows cycling performance of a Li/PI/PEO_{10}/LiTFSI/LFP cell at different charging rates, cycled at about 30 °C.

[0016] Figure 5 demonstrates abuse tests of PI/PEO/LiTFSI. Figure 5(a) shows photo images of about 2 cm^2 PI/PEO/LiTFSI solid-state electrolyte free-standing film being subjected to folding, twisting and unfolding. Figure 5(b) shows photo image of the abused PI/PEO/LiTFSI film as a solid-state electrolyte in an LFP/PI/PEO/LiTFSI/Li coin cell lighting an LED bulb Figure 5(c) Flexible Li/PI/PEO/LiTFSI/LFP pouch cell lighting an LED bulb. Figure 5(d) shows Li/PI/PEO/LiTFSI/LFP pouch cell lighting an LED bulb after nail test. Figure 5(e) showsLi/PI/PEO/LiTFSI/LFP pouch cell lighting an LED bulb after cutting.

[0017] Figure 6(a) shows photo images of a microcaliper measuring porous PI film. Figure 6(b) shows photo images of a microcaliper measuring commercial glass SSE (on the right cross-sectional SEM image of the same SSE). Figure 6(c) shows photo images of a microcaliper measuring homemade PEO/LiTFSI. Figure 6(d) shows photo images of a microcaliper measuring abuse test of porous PI film shows its intrinsic flexibility.

[0018] Figure 7(a) shows a comparison of PI/PEO/LiTFSI with state-of-the-art SSEs in literature in terms of thickness. Figure 7(b) shows a comparison of PI/PEO/LiTFSI with state-of-the-art SSEs in literature in terms of area density.

[0019] Figure 8(a) shows a top view SEM image of pristine porous PI film. Figure 8(b) shows a cross-sectional SEM image of pristine porous PI film.

[0020] Figure 9(a) shows a schematic image of EIS measurement of PI/PEO/LiTFSI with electrochemical (EC) workstation. Figure 9(b) shows top view and figure 9(c) shows side view schematic images to illustrate the size of gold deposition on porous PI thin film.

[0021] Figure 10 shows a Nyquist plot of SS/PI/PEO/LiTFSI/SS (0.16 cm^2 electrode area) tested at 20 °C, 25 °C and 30 °C.

[0022] Figure 11 shows a Nyquist plot of SS/PI/PEO/LiTFSI/SS (0.49 cm^2 electrode area) tested at 20 °C, 25 °C and 30 °C.

[0023] Figure 12(a) shows a schematic of 2D-XRD with PEO/LiTFSI in vertical aligned channels. Figure 12(b) shows a schematic of X-ray diffraction patterns collected by CCD. Figure 12(c) shows a schematic of X-ray diffraction patterns with isotropic materials and Figure 12(d) shows a schematic of X-ray diffraction patterns with highly textured materials along out-of-plane directions. Figure 12(e) shows XRD analysis of PEO/LiTFSI film and Figure 12(f) shows XRD analysis of PEO/LiTFSI in vertical aligned channels.

[0024] Figure 13(a) shows zoomed in steps of symmetric Li cells from Figure 3a. Figure 13(b) shows a second set of zoomed in steps of symmetric Li cells from Figure 3a.

[0025] Figure 14 shows Li/PI/PEO/LiTFSI/Li and Li/PEO/LiTFSI/Li symmetric cell at current density of 0.1 mA/ cm^2 at 40 °C.

[0026] Figure 15(a) shows a schematic image of Li/PI/PEO/LiTFSI/Li symmetrical cell, with Li metal coated with PEO/LiTFSI/Al_2O_3. Figure 15(b) shows voltage *vs.* time plot Li/PI/PEO/LiTFSI/Li symmetrical cell cycled at various current densities and capacities. Figure 15(c)-Figure 15(f) show a zoomed in plot of Figure 15(b) at different times with Figure 15(c) 0.1 mA/ cm^2, 0.3 mAh/ cm^2; Figure 15(d) 0.2 mA/ cm^2, 0.5 mAh/cm^2; Figure 15(e) 0.3 mA/cm^2, 0.75 mAh/cm^2; Figure 15(f) 0.4 mA/cm^2, 1 mAh/cm^2. Figure 15(g) shows a schematic image of Li/Li symmetrical cell, where Li metal coated with the same PEO/LiTFSI/Al_2O_3 film as Figure 15(a). Figure 15(h) shows voltage *vs.* time plot of Li/PI/PEO/LiTFSI/Li symmetrical cell cycled at various current densities (0.05 mA/cm^2, 0.025 mAh/cm^2; 0.1 mA/cm^2, 0.3 mA/cm^2; exactly the same program as the Li/PI/PEO/LiTFSI/Li cell before 200 hours) Figure 15(i) shows a zoomed in image of Figure 15(h),and clearly shows the short circuiting of Li/Li cells at around 6 hours with 0.05 mA/cm^2, 0.025 mAh/cm^2 cycling parameter.

[0027] Figure 16(a) shows voltage vs. time plot of Li/PI/PEO/LiTFSI/Li symmetrical cell cycled at a current density of 0.5mA/cm^2 and a capacity of 1.5mAh/cm^2, started at 500th hour. Figures 16(b- c). Zoomed in plot of Figure 16(a) at different times with one lithium plating/striping cycle.

[0028] Figure 17 shows SEM and schematic images of Li/PEO/LiTFSI/Al_2O_3 with FIB. Figure 17(a) shows a SEM top view of the Li/PEO/LiTFSI/Al_2O_3. Figure 17(b) shows a zoomed-in and tilted view of Figure 17(a). Figure 17(c) shows a further zoomed-in figure from yellow box in Figure 17(b), where the dashed line separates three regions, cross section of bulk Li, cross section of PEO/LiTFSI/Al_2O_3, and top surface of PEO/LiTFSI/Al_2O_3 (from bottom to top), respectively Figure 17(d) schematic image of a 3D illustration of Figure 17(c), the grey area represent bulk Li, dark green represent PEO/LiTFSI/Al_2O_3 (cross section) and light green represent PEO/LiTFSI/Al_2O_3 (top surface).

[0029] Figure 18(a-b) shows SEM images of pristine PI film and Figure 18(c-d) shows SEM images of pristine PI film after cycling with current density of 0.5mA/cm^2 and areal capacity of 1.5mAh/cm^2 in a Li-Li symmetrical cell.

[0030] Figure 19 shows a full set of SEM images (with different magnifications) of PI film after cycling with current density of 0.5 mA/cm^2 and areal capacity of 1.5 mAh/cm^2 in a Li-Li symmetrical cell. (figures 19d and 19g are the same from figures 18c and 18d).

[0031] Figure 20(a) shows a schematic image of the current density redistribution model in the sandwiched structure. Figure 20(b) Li ion concentration distribution at steady state (time=100s) with current density of 0.4 mA/cm^2.

[0032] Figure 21(a) shows a simulation result of current distribution in the two PEO/Al_2O_3 sandwiching PI/PEO/LiTFSI structure, the plot is zoomed in the regions of 2 μm PEO/Al_2O_3 and part of PI/PEO/LiTFSI. Figure 21(b) shows current density taken at 1 μm deep, marked in red line in the schematic inset Figure 21(c) simulation result of current distribution in the two PEO/Al_2O_3 sandwiching PI/PEO/LiTFSI structure, the plot is zoomed in the regions of 0.3 μm PEO/Al_2O_3 and part of PI/PEO/LiTFSI. Figure 21(d) shows current density taken at 0.3 μm deep, marked in red line in the schematic inset.

[0033] Figure 22 shows evolution snapshots at different time steps from phase-field simulation of Li electrodeposition near the PEO/LiTFSI channel: Figures 22(a-f) show multiphase morphologies, Figures 22(g-l) show Li ion concentration distributions, and Figures 22(m-r) show electrostatic overpotential profiles.

[0034] Figure 23 shows the phase-field evolution driving forces contribution during Li electrodeposition.

[0035] Figure 24(a) shows SEM image of Li deposited on a flat copper substrate. Figure 24(b) shows statistics of Li protrusion size from Figure 24(a).

[0036] Figure 25 shows evidence for Li protrusions. Figure 25(a) is an SEM image of a Li protrusion deposited under PI/PEO/LiTFSI electrolyte. Figure 25(b) is an SEM image of Figure 25(a) after FIB cutting; Figure 25(c) is an SEM image of another Li protrusion after FIB; Figure 25(d) is an SEM image of Figure 25(c) in BSE mode; Figure 25(e-g) are SEM images of multiple Li protrusions after FIB.

[0037] Figure 26 shows cycling performance of LFP/PI/PEO/LiTFSI/Li cell at 40 °C.

[0038] Figure 27 shows voltage profile of LFP/PI/PEO/LiTFSI/Li cell at 40 °C at C/5.

[0039] Figure 28(a) shows a voltage profile and Figure 28(b) shows cycling performance of LFP/PI/PEO/LiTFSI/Li at 30°C and a rate of C/10.

[0040] Figure 29(a) shows cycling performance of high cathode loading LFP/PI/PEO/$LiTFSI_{10}$/Li batteries (LFP loading of 6.9 mg/cm^2 and 3.9 mg/cm^2) running at 40 °C. Voltage profiles of the cathode loading of Figure 29(b) 6.9 mg/cm^2 and Figure 29(c) 3.9 mg/cm^2 batteries.

Detailed Description

[0041] The demand for safer batteries is prompting the development of all-solid-state lithium-based cells. To achieve energy density comparable to liquid electrolyte-based cells, ultrathin and lightweight solid electrolytes with yet high ionic conductivity are desired. However, solid electrolytes with comparable thicknesses of commercial polymer electrolyte separators (about 10 μm) used in liquid electrolyte remain challenging to form because of the increased risk of short circuiting the battery. Here some embodiments are directed to an improved structural design, demonstrated with about 8.6 μm thick nanoporous polyimide (PI) film, filled with polyethylene oxide/lithium bis(trifluoromethanesulfonyl)imide (PEO/LiTFSI) as a safe solid polymer electrolyte. The PI film is nonflammable and mechanically strong, preventing batteries from short circuiting even after more than 1000 h of cycling, while vertical channels enhance the ionic conductivity (e.g., about 2.3× 10^{-4} S/cm at about 30 °C) of the infused polymer electrolyte. All-solid-state lithium-ion batteries fabricated with PI/PEO/LiTFSI solid electrolyte show good cycling performance (e.g., 200 cycles at C/2 rate) at about 60 °C and withstand abuse tests such as bending, cutting, and nail penetration.

Composite solid electrolyte

[0042] In one aspect, the present disclosure includes a composite solid electrolyte. For instance, some embodiments include a composite solid electrolyte comprising: a porous matrix having channels; and ionically conducting fillers disposed within the channels.

[0043] The composition of the porous matrix is not particularly limited. In some embodiments, the porous matrix is compatible as a solid electrolyte or in a battery of other similar device. Certain embodiments include where the porous matrix comprises or consists of a porous polymeric matrix. In some embodiments, the polymeric matrix comprises or consists of a porous polymeric film or layer. In some embodiments, the porous polymeric matrix is a porous inorganic film/matrix (with Li ion conducting ceramics (e.g. $Li_7La_3Zr_2O_{12}$, $Li_{10}GeP_2S_{12}$, Li_3InCl_6, $Li_{3x}La_{2/3-x}TiO_3$, including their derivatives and combinations (see, e.g. J. Bachman, Chemical Reviews, 2016, 116, 140-162) or nonconducting inorganics (Al_2O_3. SiO_2, TiO_2, Sb_2O_5, and other metal oxides, metal sulfides, metal fluorides, and metal chlorides, including their derivatives and combinations. In some embodiments, the porous polymeric matrix has a thickness of about 100 μm or less, such as 100, 95, 90, 85, 80, 75, 70, 65, 60, 55, 50, 45, 40, 35, 30, 25, 20, 15, 14, 13, 12, 11, 10, 9, 8, 7 μm or less.

[0044] Certain embodiments, include where the porous polymeric film or layer has a first major surface and an opposite, second major surface, and the channels extend at least partially through a thickness of the porous polymeric film between the first surface and the second surface. In some embodiments, at least a portion of the channels extend partially through a thickness of the porous polymeric film between the first surface and the second surface, e.g., at least 5, 10, 20, 30, 40, 50, 60 , 70, 80, 90, 95, 98, 99, 99.5, or 100% extend partially. In some embodiments, at least a portion of the channels extend fully through a thickness of the porous polymeric film between the first surface and the second surface, e.g., at least 10, 20, 30, 40, 50, 60 , 70, 80, 90, 95, 98, 99, 99.5, or 100% extend fully. In some embodiments, the remaining channels that do not extend fully still extend partially. In some embodiments, the channels have lateral dimensions or widths in a range of about 0.1 nm, about 0.5 nm, or about 1 nm to about 1000 nm, about 1500 nm, or about 2000 nm. For instance, in some embodiments, the channels have lateral dimension (in nm) of about 0.1 nm, 0.5 nm, and any integer between 1 and 1000, or a range therein between. For example, in some embodiments, the channels have lateral dimensions or widths up to about 900 nm or

less, up to about 800 nm or less, up to about 700 nm or less, up to about 600 nm or less, up to about 500 nm or less, up to about 400 nm or less, or up to about 300 nm or less, and down to about 200 nm or less, or down to about 100 nm or less.

[0045] Certain embodiments include where the channels have a particular configuration. In some embodiments, the channels are configured to have a soft-nanochannel/hard-matrix unit(s), where these soft-nanochannel portions can each independently have a dimension from about 0.1 nm to about 2000 nm. In some embodiments, the soft-nanochannel/hard-matrix unit(s) are repeating units with each repeat unit independently has a dimension from about 0.1 nm to about 2000 nm. In some embodiments, the soft-nanochannel/hard-matrix unit(s) are randomly distributed, and each unit independently has a dimension from about 0.1 nm to about 2000 nm. In some embodiments, the dimension of the soft-nanochannel portions in the soft-nanochannel/hard-matrix unit(s) reduces or prevents short circuiting when in a battery. In some embodiments, the soft-nanochannel/hard-matrix unit(s) interconnected 3D networks of soft nanochannels that are within a dimension from about 0.1 nm to about 2000 nm (from the top view). In some embodiments, the soft-nanochannel/hard-matrix repeating units have an alignment direction. An example of this soft-nanochannel/hard-matrix repeating unit configuration is shown in embodiments of the Figures. For instance, in some embodiments, the alignment direction is specified as orthogonal to the first surface or the second surface, and at least some of the channels extend between the first surface and the second surface along respective longitudinally extending directions that are within ±35° of the alignment direction. For example, in some embodiments, at least 10, 20, 30, 40, 50, 60, 70, 80, 90, 95, 98, 99, 99.5, or 100% of the channels extend between the first surface and the second surface along respective longitudinally extending directions that are within ±35° (e.g., within ±35, 30, 25, 20, 15, 14, 13, 12, 11, 10, 9, 8, 7, 6, 5, 4, 3, 2, 1, or 0) of the alignment direction.

[0046] Certain embodiments include a specific elastic modulus for the porous matrix. In some embodiments, the porous matrix has an elastic modulus (or Young's modulus) of about 10 MPa or greater, about 50 MPa or greater, about 100 MPa or greater, about 200 MPa or greater, about 300 MPa or greater, about 400 MPa or greater, about 500 MPa or greater, about 600 MPa or greater, about 700 MPa or greater, or about 800 MPa or greater, and up to about 1000 MPa or greater. In some embodiments, the porous matrix has an elastic modulus (or Young's modulus) of less than 200 MPa, or it has an elastic modulus (or Young's modulus) within the values of any two of about 10 MPa, about 50 MPa, about 100 MPa,

about 200 MPa, about 300 MPa, about 400 MPa, about 500 MPa, about 600 MPa, about 700 MPa, about 800 MPa, about 1000 MPa, about 1500 MPa, and about 2000 MPa.

[0047] The composition of the porous polymeric film or layer is not particularly limited. In some embodiments, the porous polymeric film or layer is compatible as a solid electrolyte or in a battery of other similar device. In some embodiments, the porous polymeric film or layer comprises a uniform mixture of a solid polymer. Examples of suitable polymers include, but are not limited to polyimides or another polymer or mixture of polymers that are nonflammable and mechanically strong. Additional non-limiting embodiments, polytetrafluoroethylene (PTFE), polyacrylonitrile (PAN), nylon, polyethylene, polypropylene, polystyrene, kevlar, and the like. In some embodiments, the porous polymeric matrix is a porous inorganic film/matrix (with Li ion conducting ceramics (e.g., $Li_7La_3Zr_2O_{12}$, $Li_{10}GeP_2S_{12}$, Li_3InCl_6, $Li_{3x}La_{2/3-x}TiO_3$, and their derivatives or combinations thereof (see, e.g., J. Bachman, Chemical Reviews, 2016, 116, 140-162) or nonconducting inorganics, such as, Al_2O_3. SiO_2, TiO_2, Sb_2O_5, other metal oxides, metal sulfides, metal fluorides, and metal chlorides, including their derivatives and combinations thereof), or organic/inorganic hybrid (of, e.g., the above materials) matrix.

[0048] In some aspects, the ionically conducting fillers include a solid polymer electrolyte. For instance, the solid polymer electrolyte can include a polymer and a lithium-containing salt. In some embodiments, the solid polymer electrolyte includes a polymer that comprises a polyether, such as polyethylene oxide and its derivatives (e.g., in J. Mater. Chem. A, 2015, 3, 38), poly(propylene carbonate), poly(vinylene carbonate), polyacrylonitrile (PAN), other Li-conducting polymers, their derivatives and combinations (see, e.g., Kang Xu, Chemical Reviews, 2014, 114, 23, 11503-11618; Kang Xu, Chemical Reviews, 2004, 104, 10, 4303-4417). In some embodiments, the polymer, e.g., PEO, has a weight average molecular weight (Mw) equal to or greater than about 5000, 10000, 15000, 20000, 25000, 30000, 40000, 50000, 100000, 150000, 200000, 250000, 30000, 350000, 400000.

[0049] The lithium-containing salt is not particularly limited, and embodiments include, e.g., a Li-salt containing a fluorinated counterion, such as, bis(trifluoromethanesulfonyl)imide, lithium hexafluorophosphate, Li perchlorate, Li bis(fluorosulfonyl)imide, Li nitrate, Li bis(oxalato)borate, and the like, and/or their combinations (see, g.g., Kang Xu, Chemical

Reviews, 2014, 114, 23, 11503-11618; Kang Xu, Chemical Reviews, 2004, 104, 10, 4303-4417).

[0050] In some embodiments, the ionically conducting filler to Li ratio is about 20:1 or less, about 18:1 or less, about 16:1 or less, about 14:1 or less, about 12:1 or less, or about 10:1 or less, down to about 8:1 or less, down to about 5:1 or less, down to about 2:1 or less. For instance, in some embodiments, the polymer in the solid polymer electrolyte is polyethylene oxide and/or its derivatives, and an ethylene oxide (EO) to Li ratio is about 20:1 or less, about 18:1 or less, about 16:1 or less, about 14:1 or less, about 12:1 or less, or about 10:1 or less, down to about 8:1 or less, down to about 5:1 or less, down to about 2:1 or less.

Batteries

[0051] Other aspects of the present disclosure include lithium batteries (e.g., solid-state lithium batteries) containing a composite solid electrolyte of any of the foregoing embodiments. In some embodiments, the solid-state lithium battery comprises a cathode; an anode; and a composite solid electrolyte of any of the foregoing embodiments disposed between the cathode and the anode.

[0052] The anode and cathode materials are not particularly limited as long as they are compatable with the lithium batteries of the disclosure. In some embodiments, the anode is metallic, e.g., an anode that includes metallic lithium. In some embodiments, the cathode includes a transition metal oxide as a cathode active material, such as lithium cobalt oxide ($LiCoO_2$), lithium manganese oxide ($LiMn_2O_4$), lithium nickel manganese cobalt oxide ($LiNi_xMn_yCo_zO_2$), or lithium iron phosphate ($LiFePO_4$).

[0053] In some embodiments, the battery further comprises an active material, such as $LiFePO_4$ (LFP) active material. In some embodiments, the active material loading is about 1 mg/cm^2 or more, e.g., about 1, 1.5, 2, 3, 4, 5, 6, 7, 8, 9, or 10 mg/cm^2.

[0054] In certain aspects, the batteries show good cycling performance and/or withstand abuse tests. In some embodiments, the battery performs at least 200 cycles at C/2 rate) at about 60 ºC. In some embodiments, the battery withstands bending, cutting, and/or nail penetration.

Method of Making

[0055] Other aspects of the present disclosure are directed to a manufacturing method of a composite solid electrolyte, which includes providing a porous matrix having or defining channels, infusing or infiltrating a solution of a polymer and a lithium-containing salt into the channels of the porous matrix, and heating the infused or infiltrated porous matrix to form the composite solid electrolyte. In some embodiments, providing the porous matrix include subjecting a matrix to track etching (directing an ion beam, followed by wet chemical etching) to form the channels in the porous matrix.

[0056] Other aspects and embodiments of this disclosure are also contemplated. The foregoing detailed description and the following Additional embodiments are not meant to restrict this disclosure to any particular embodiment but are merely meant to describe some embodiments of this disclosure.

Additional embodiments

[0057] In some embodiments, a design of ultrathin, high performance polymer-polymer composite solid electrolytes of the present disclosure is utilized for all-solid-state lithium batteries. (Figure 1a) In some embodiments, the composite SSE is formed of a robust, nonflammable host with vertically aligned nanochannels and Li-ion conductive SPE fillers. The high modulus host may prevent potential dendrite penetration while the aligned channels may enhance the ionic conductivity of the SPE fillers. The ultrathin and polymer-polymer nature of the composite electrolyte provides great flexibility, low electrolyte resistance, and potential high energy density of a full battery.

[0058] High modulus, nanoporous polyimide hosts and PEO/LiTFSI polymer electrolytes are utilized as an example polymer-polymer SSE for the design (also in Figure 6). Cross-sectional scanning electron microscopy (SEM) images of the ultrathin, porous PI matrix are shown in Figure 1b, where the thickness is identified to be about 8.6 μm (Figure 1b, bottom). The vertical nanoporous morphology of PI is zoomed in and shown in Figure 1b (top). A photo image of a large-scale, nanoporous, and flexible PI film is shown in Figure 1c, demonstrating the scalability of such composite system. Comparison is made of the energy densities of state-of-the-art LIBs with both liquid electrolyte and various solid electrolytes in Figure 1d, to illustrate the advantage of the polymer-polymer SPE. Although the theoretical energy density of commercial Li-ion battery approaches 480 Wh/kg, it decreases by about

half if metal casing, cathode current collector (e.g., Al) and anode current collector (e.g., Cu) are considered in the calculation (column A). The energy density further decreases when separators and liquid electrolyte are taken into consideration (column B). However, the energy densities of all-solid-state cells are comparable to those of liquid electrolyte cells if the PI/PEO/LiTFSI electrolyte is utilized (about 246 Wh/kg), and much higher than other state-of-the-art all-solid-state batteries (more details in Table 1 and Figure 7). The thin, ultralight PI/PEO/LiTFSI obtains a similar area density (about 1.12 mg/cm^2) compared with separator/liquid electrolyte (about 1 mg/cm^2), ensuring its advantage over other solid electrolyte systems (also see Figure 7). Energy densities of solid polymer-polymer composite Li-ion batteries could potentially reach the upper area in column A, as cell casing for all-solid-state LIBs can be more streamlined than Li-ion batteries with liquid electrolytes. Even higher energy densities can potentially be realized through high capacity Li chemistries, such as sulfur and metallic lithium.

Characterizations of PEO/LiTFSI in porous PI

[0059] SEM images before and after the infiltration of PEO/LiTFSI polymer electrolyte into the PI film are presented in Figures 2a-d. Figure 2a shows a top-view image of the porous PI film in which the pores are uniformly distributed (zoomed out image in Figure 8) with diameters of about 200 nm. These images show that the pores occupy about 11% of the area on the PI surface. After PEO/LiTFSI infiltration, the pores are substantially completely filled with PEO/LiTFSI and serve as the Li-ion conductive medium (Figure 2b). Cross-sectional SEM images of the porous PI film (Figure 2c) and filled PI/PEO/LiTFSI film (Figure 2d) also demonstrate the substantially complete infiltration of PEO/LiTFSI in the vertical pores. The ionic conductivities of the SSEs were measured using blocking cells from about -20 °C to about 100 °C. The PEO/LiTFSI in the PI vertical channels is measured to have enhanced ionic conductivity as compared to that of PEO/LiTFSI thin film across all measurement temperatures (Figure 2e, also Figures 9-11). Specifically, the PEO/LiTFSI in aligned channels shows ionic conductivity of about 2.3×10^{-4} S/cm at about 30 °C, whereas the PEO/LiTFSI thin film shows conductivity of about 5.4×10^{-5} S/cm (about 30 °C). The electrochemical impedance spectroscopy curves of PI/PEO/LiTFSI at different temperatures are plotted in Figure 2f.

[0060] To investigate the effect that the vertical channels may have on PEO/LiTFSI, a two-dimensional X-ray Diffraction (2D-XRD) characterization is conducted of the PEO/LiTFSI electrolyte and PEO/LiTFSI filled in vertically aligned 200 nm channels. In Figures 2g and 2h, the ring diffraction patterns with blue and green arrows that appear in the composites are attributed to the (1 2 0) and (1 1 2) planes of the PEO crystallites, respectively. The PEO/LiTFSI thin film sample shows an isotropic ring pattern (Figure 2g), revealing an isotropic distribution of the crystallites. In contrast, Figure 2h shows the PEO/LiTFSI in the vertical channels with a concentrated intensity on the y-axis, which represents a textured distribution of crystallites along the out-of-plane direction. This indicates that the channels inside the matrix help align the PEO crystallites along them (more details see Figure 12). Similar alignment effects on polymers lead to thermal or ionic transport enhancement in the aligned direction, both of which are related to vibration of polymer chains (Singh, V. et al. High thermal conductivity of chain-oriented amorphous polythiophene. *Nat. Nanotech.* **9,** 384–390 (2014); Jo, G., Ahn, H. & Park, M. J. Simple route for tuning the morphology and conductivity of polymer electrolytes: One end functional group is enough. *ACS Macro Lett.* **2,** 990–995 (2013)).

[0061] Molecular dynamics (MD) simulations are carried out to explore the reason for enhanced ionic conductivity. In the simulations, PEO/LiTFSI with random and aligned polymer chains are compared to show the difference in Li ionic conductivity. The simulation snapshots of the two systems are shown in Figure 2i (PEO with randomly-oriented chains and Li salts) and Figure 2j (PEO with aligned chains and Li salts). Mean squared displacements (MSD) of lithium ions in both aligned and random PEO matrices at 350 K are calculated and displayed in Figure 2k. The MSDs in different directions for the random chain PEO system show little difference, and the values are comparable with reported results (e.g., Webb, M. A. et al., Systematic computational and experimental investigation of lithium-ion transport mechanisms in polyester-based polymer electrolytes. *ACS Cent. Sci.* **1,** 198–205 (2015); Sethuraman, V., et al., Ion transport mechanisms in lamellar phases of salt-doped PS–PEO block copolymer electrolytes. *Soft Matter* **13,** 7793–7803 (2017)). In contrast, a clear increase in Li^+ diffusion is found along the aligned direction (z) in comparison to all directions from the randomly-oriented PEO/LiTFSI sample. The ionic diffusion along the aligned direction shows an even bigger difference to those in the other two directions (x and y) in the aligned PEO/LiTFSI system. Based on the simulation results, Li-ion optimize a diffusion path along

the alignment direction. The diffusion coefficients for each system are calculated based on the slope of the MSD between 25 ns to 35 ns (inset of Figure 2k). The diffusivity of the aligned z direction is 1.3 x 10^{-8} cm^2/s, while the average diffusivity in the random system is 5.7 x 10^{-9} cm^2/s. The MD simulations show that polymer chain alignment is beneficial to ion diffusion in the alignment direction, providing a possible explanation for the enhanced ionic conductivity of PI/PEO/LiTFSI in the aligned channels. This explanation is consistent with stretching-induced ionic conductivity enhancement in polymer electrolytes. This ionic conductivity enhancement of PEO/LiTFSI in aligned nanochannels may be attributed to the nanoconfinement effects of channels and/or polymer chain alignment at SPE/channel interfaces (e.g., Liu, W. et al., Enhancing ionic conductivity in composite polymer electrolytes with well-aligned ceramic nanowires. *Nat. Energy* **2**, 17035 (2017); Xue, Z., et al., Poly(ethylene oxide)-based electrolytes for lithium-ion batteries. *J. Mater. Chem. A* **3,** 19218–19253 (2015); Toney, M. F. et al. Near-surface alignment of polymers in rubbed films. Nature **374**, 709-711 (1995)); other advanced techniques such as solid-state NMR (e.g., Zheng, J., Tang, M. & Hu, Y. Y. Lithium Ion Pathway within $Li_7La_3Zr_2O_{12}$-Polyethylene Oxide Composite Electrolytes. *Angew. Chem. Int. Ed.* **55,** 12538–12542 (2016)) or Neutron depth profiling (e.g., Wang, C. et al. In Situ Neutron Depth Profiling of Lithium Metal-Garnet Interfaces for Solid State Batteries. *J. Am. Chem. Soc.* **139**, 14257–14264 (2017)) can more thoroughly characterize the contributing factors of this effect.

Electrochemical tests of PI/PEO/LiTFSI electrolyte

[0062] Li/SPE/Li symmetric cells are fabricated to evaluate the mechanical stability of the PI/PEO/LiTFSI SPE during the Li plating and stripping process. The cycling tests were carried out at about 60 °C, as shown in Figure 3a (zoomed in plot shown in inset, also Figure 13; more Li-Li tests in Figures 14-16). Under a current density of about 0.1 mA/cm^2, a hard short occurred in a very short time (less than about 40 h) in plain PEO cells. Despite the PEO/LiTFSI thin film being much thicker (about 130 μm) than the ultrathin PI/PEO/LiTFSI SPE, the latter demonstrated more stable performance during Li plating/stripping, lasting about 1000 h at about 60 °C. Stress-strain curves of PEO/LiTFSI and porous PI obtained through tensile tests are plotted in Figure 3b. The porous PI shows a much larger modulus of about 850 MPa, which is almost 5 orders of magnitude higher than that of PEO/LiTFSI (about 0.1 MPa). Figures 3c and 3d compare the Li deposition morphology with EC/DEC/$LiPF_6$ liquid electrolyte and PI/PEO/LiTFSI SPE (under the same Li plating

conditions), respectively. Noticeable dendrite formation is observed with the liquid electrolyte, while suppressed Li protrusion formation is observed with the PI/PEO/LiTFSI SPE. Note that the Li protrusions under PI/PEO/LiTFSI have diameters of a few microns, in contrast to dendrites of a few hundred nanometers from $LiPF_6$/EC/DEC. This phenomenon indicates that the deposited Li does not tend to penetrate the soft channel region, but rather pushes forward the composite electrolyte as a whole. The suppressed Li dendrite growth results from the increased modulus of the PI/PEO/LiTFSI SPE, explaining the long, durable performance and stability of PI/PEO/LiTFSI SPE during Li stripping/plating (also see Figures 15-25). This success also indicates the potential of the proposed high modulus matrix/high ionic conductivity filler structures to prevent dendrite formation. Moreover, the PI host is flame retardant, whereas pure PEO/LiTFSI ignites readily. (Figure 3e).

[0063] Testing is conducted of the PI/PEO/LiTFSI film as an SSE in all-solid-state Li-ion batteries. The coin cells were made with $LiFePO_4$ (LFP) cathodes, PI/PEO/LiTFSI as the solid electrolytes and Li metal as the anodes. Control cells were made with the same cathodes and anodes, but using PEO/LiTFSI as the solid electrolytes instead. The thickness of PEO/LiTFSI is about 150 μm to prevent short circuits during cycling at initial stages. The PI/PEO/LiTFSI cells were tested at about 60 °C and delivered excellent rate performance. Voltage profiles (Figure 4a) at different rates show clear plateaus at about 3.45 V, which is typical for LFP cathodes. Note that the ultrathin PI/PEO/LiTFSI cell maintains very low overpotentials of about 55 mV and about 42 mV at C/5 and C/10 rates, respectively. Even at C/2, the overpotential of LFP/PI/PEO/LiTFSI/Li is about 100 mV, reflecting the thin nature of the PI/PEO/LiTFSI film. In contrast, a relatively large overpotential of about 86 mV is observed at C/10 for LFP/PEO/LiTFSI/Li. When cycling these cells at C/10, C/5, C/2 and 1C, the LFP/PI/PEO/LiTFSI/Li all-solid-state LIB delivered high specific capacities of about 176 mAh/g, about 156 mAh/g, about 138 mAh/g, and about 125 mAh/g, respectively (Figure 4b). The LFP/PI/PEO/LiTFSI/Li cell also shows very stable cycling for more than 200 cycles at C/2, whereas the LFP/PEO/LiTFSI/Li cell decays dramatically within 100 cycles (Figure 4c). Similarly demonstrated is that the LFP/PI/PEO/LiTFSI/Li cells can be stably cycled at lower temperatures of about 40 °C and about 30 °C with capacity larger than about 120 mAh/g. When a lower molecular weight PEO (Mw=10,000, polymer-polymer solid electrolyte specified as PI/PEO_{10}/LiTFSI) is used, the LFP/PI/PEO_{10}/LiTFSI/Li can be cycled at about 30 °C and still obtains a stable specific capacity of about 100 mAh/g at a fast charging rate of

C/2 (Figure 4d and 4e, more cycling performance also see Figures 26-29). Thus an SSE with vertically aligned structures is made and tested in a full cell configuration.

Abuse tests of PI/PEO/LiTFSI in full cells

[0064] After folding and unfolding, the PI/PEO/LiTFSI SPE was able to regain its original shape and functioned properly within an LFP/PI/PEO/LiTFSI/Li coin cell (Figures 5a and 5b). Pouch-type cells of LFP/PI/PEO/LiTFSI/Li were made to verify the flexibility of the all-solid-state LIB. As shown in Figure 5c, the all-solid-state pouch cell is connected to a red light-emitting diode (LED). When twisted or folded, the LED remained lit, demonstrating the good flexibility of the PI/PEO/LiTFSI all-solid-state battery. Abuse tests such as nail tests and cutting tests were also carried out with pouch type LFP/PI/PEO/LiTFSI/Li all-solid-state batteries. After the nail test (Figure 5d), the solid-state pouch cell stays safe (unlike typical LIBs, which often violently combust after such abuse) and also remains operational (shortly afterwards) and lights up the LED bulb. The PI/PEO/LiTFSI pouch cell can also still light up the LED even after the cell is cut in half.

[0065] Compared to other types of SSEs, the ultrathin nature of the polymer-polymer hybrid SSE leads to a high energy density. The processability and flexibility of the polymer composite SSEs makes it attractive to pair them with Li-ion battery production. Although the ionic conductivities of composite type SSEs are comparable to some of the ceramic SSEs (such as garnet type SSE, about 10^{-4} S/cm at room temperature), they are still behind those of sulfide based SSEs (about 10^{-3}-10^{-2} S/cm), and liquid electrolyte cells (about 10^{-2} S/cm). Thus, battery performance with composite electrolytes cycling at high current density at moderate (about 25 °C-40 °C) temperature can be further improved. Further improving the performance of composite SSEs can include (1) further enhancing their intrinsic ionic conductivities; (2) increasing effective ionic conduction pathways (such as adding more ion conducting channels) in the SSE; (3) lessening the interphase resistance (cathode/electrolyte, anode (Li metal)/electrolyte); (4) using mechanically strong, chemically/electrochemically stable materials (at least can be stabilized at the electrolyte/electrode interface) to obtain composite SSEs with reduced thickness, while remaining able to prevent short-circuiting of the battery; and (5) designing smart battery configurations to run batteries at elevated temperature with reduced energy loss through thermal conduction.

[0066] In some embodiments, demonstration is made of a composite all-solid-state electrolyte with an ultrathin, flexible, mechanically strong, nonflammable, and porous PI film as the host and PEO/LiTFSI as the ionically conducting filler. Compared to PEO/Li salt-based solid polymer electrolytes, the hybrid electrolyte has five orders of magnitude higher modulus and enhanced ionic conductivity. Thus, the hybrid PI/PEO solid electrolyte demonstrates cycling stability superior to that of PEO in Li/SPE/Li cells under identical current density. Furthermore, in LFP/SPE/Li full cells, the rate performance and cycling stability of the PI/PEO/LiTFSI SPE is also better than that of PEO/LiTFSI. LFP/PI/PEO/LiTFSI/Li all-solid-state pouch cells also demonstrate high tolerance to abuses such as bending, twisting, cutting and nail perforation. Thus, the proposed polymer-polymer composite SPE configuration represents a route to make LIBs that are safe, high energy density, high performing, and flexible.

Methods

[0067] *Preparation of solid polymer electrolyte* Polyethylene oxide (PEO, MW=300,000, Sigma Aldrich) is mixed with LiTFSI (Solvay Inc.) and acetonitrile (anhydrous, Sigma Aldrich) with a Thinky mixer (Thinky Cooperation). The ethylene oxide (EO) to Li ratio is about 10:1. Pure PEO-LiTFSI films are prepared by doctor blade casting followed by drying in a vacuum oven at about 60 °C for about 24 h and baking in Ar filled glove box at about 100 °C for at least about 48 h. The porous PI films are fabricated with track etch technique from thin Kapton polyimide films. This technique can be generally applied to obtain aligned channels in a number of other polymer systems. PI/PEO/LiTFSI solid electrolytes are obtained in a facile two-stage process. First, as prepared PEO/LiTFSI/Acetonitrile solution drops are spun at about 4000 rpm with porous PI film. The as-prepared PI/PEO/LiTFSI film is then baked at about 200 °C under vacuum to ensure the full infiltration of PEO/LiTFSI in the about 200 nm pores. The excess PEO/LiTFSI was scraped off at about 150 °C on a hot plate. The PI/PEO/LiTFSI film then underwent the same drying process as the regular PEO/LiTFSI film.

[0068] *Preparation of other battery components* $LiFePO_4$ (LFP) powders (MTI Inc.), PEO/LiTFSI, carbon black (w:w:w=about 60:25:15) were mixed in acetonitrile with a Thinky mixer. The LFP active material loading is about 1.5 mg/cm^2 (high cathode loading results see Figure 29). The slurry is then doctor blade casted on Al foil. The electrode is then dried in an

about 60 °C vacuum oven for at least about 48 h. Coin cells (2032 type, MTI Inc.) were made either with Li-SPE-Li or Li-SPE-LFP type cells. Lithium foil is obtained from Sigma Aldrich.

[0069] *Materials Characterizations* SEM images are taken with a FEI XL30 Sirion SEM. Mechanical test are taken with TA instrument Q800 DMA. 2D-XRD data is obtained with Bruker D8 Venture system.

[0070] *Electrochemical characterizations* Ionic conductivity measurements are obtained with symmetrical SS/SPE/SS structure in coin cells (2032 type). Electrochemical measurements such as electrochemical impedance spectroscopy (EIS) and cycling tests are carried out with Bio-logic VMP3 and LAND systems. All temperature-controlled experiments are tested inside an environmental chamber (BTU-133, ESPEC North America, Inc.) with high precision thermometer (± 0.1°C).

[0071] *Molecular dynamics simulation* For all MD simulations, Optimized Potentials for Liquid Simulations all atom (OPLS-AA) force field is used to describe PEO, Li-ion and $TFSI^-$. The atomic charges of the PEO monomer are calculated using density functional theory (DFT) based on an oligomer consisting of 5 EO monomers. The DFT calculations use the Becke exchange plus Lee-Yang-Parr functional (B3LYP) and 6-311++g(d,p) basis sets, and are conducted using GAUSSIAN 09. The atomic partial charges are estimated by matching the electrostatic potentials from DFT calculations. All simulations are performed using the Gromacs simulation package. The equations of motion are evolved using the velocity-Verlet integrator with a 2 fs time step. A cutoff of 12 Å is used to calculate both LJ interactions and electrostatic interactions, and the particle-mesh Ewald method is used to evaluate the long-range electrostatic interactions with a grid spacing of 1.2 Å. The temperature is controlled using the Nosé–Hoover thermostat with a relaxation time of 0.2 ps. For each system, a fixed number of PEO chains, cations, and anions are loaded into a simulation box with a low density of about 0.1 g/cm^3. The system is subjected to compression in a 1 ns simulation with pressure coupled to 1000 bar at 500 K. A further 10 ns equilibration in NPT ensemble at 1 bar, 350K is conducted to achieve equilibrated density. To build the randomly mixed mixture, after NPT equilibration, the non-bonded interaction of the system is turned off and an NVT simulation is conducted for 10 ns. For the aligned PEO system, during the NVT simulation without non-bonded interactions, a force of 1000 kJ/(mol·nm) is applied

to both ends of each chain in opposite directions. After 50 ns equilibration in NVT ensemble, a production run of 70 ns in NVT ensemble is further conducted to examine ion diffusion behavior.

[0072] Figures 6a-c show the drastic differences between ultrathin PI matrix and other SSE (commercial glass SSE and custom-made PEO/LiTFSI). Figure 6d shows that the flexible, porous PI film can endure various abuse tests, such as folding and twisting. Notably, the nanoporous PI film shows outstanding flexibility, returning to its original shape after folding and crushing instead of breaking. (Figure 6) The mechanically strong, highly flexible, ultrathin matrix prevents potential short-circuiting issues for LIBs, and also demonstrates the facile fabrication of flexible all-solid-state electrolytes. Detailed information regarding the thickness, density, and areal density of the proposed SSE, alongside the energy densities of other representative SSEs (of Figure 1d) is summarized in Table 1. For a fair comparison of the energy densities achievable with different solid electrolytes, the calculation parameters (such as area energy density, cell level energy density and so forth) are chosen based on commercial Panasonic 18650 Li-ion batteries (Lin, D., Liu, Y. & Cui, Y. Reviving the lithium metal anode for high-energy batteries. *Nature Nanotechnology* **12,** 194–206 (2017)). For PEO hybrid solid electrolyte, PEO/SiO_2 (with a thickness of about 200 μm and a density of about 1.5 g/cm^3) is chosen as a representative candidate. For ceramic solid electrolytes, two representative candidates are chosen: LLZO and LGPS. The thickness and density of LLZO solid electrolyte is about 200 μm and about 5.0 g/cm^3, respectively, while those of LGPS are about 240 μm and about 2.94 g/cm^3.

[0073] The utilization of lightweight solid-state electrolytes is desired to the creation of all solid-state batteries with high energy density. Designing solid-state electrolyte materials with low thickness and density can effectively lead to overall low areal density. The energy density calculation (Table 1) shows the massive improvement of PI/PEO/LiTFSI (about 244 Wh/kg) over both PEO/SiO_2 hybrid electrolytes (D3, about 58 Wh/kg) and ceramic based electrolytes (E2, E3, < about 30 Wh/kg, with minimum thickness of about 200 μm). The energy densities of the thinnest ceramic (E1) and composite type SSEs (D1, D2) reported are about 150 Wh/kg -- still significantly lower than that of PI/PEO/LiTFSI. Figure 7 is plotted based on the information provided in Table 1, where C, D1-D3 (polymer ceramic hybrid type SSEs) and E1-E3 (ceramic type SSEs) labeled in Figure 1 also correspond to the SSEs listed in Table 1. Figure 7a compares the thickness of the PI/PEO/LiTFSI to other SSEs, showing

that the about 8.6 μm thickness is the thinnest among all SSEs. Figure 7b shows the calculated area densities of all SSEs. Together with Figure 1g and Table 1, the comparison demonstrates the advantage of the ultrathin PI/PEO/LiTFSI SSEs in achieving high energy density for all-solid-state lithium batteries.

[0074] Figure 8a shows a top view SEM image of the porous PI film with uniformly distributed channels. The areal porosity of the PI film is measured with "ImageJ" software as about 11%. The cross-sectional image of Figure 8b shows the vertically aligned channels through the porous PI film.

[0075] To obtain the true ionic conductivity of PEO/LiTFSI in the channels, the preparation process of the PI/PEO/LiTFSI for EIS measurement was slightly different from that of the regular PI/PEO/LiTFSI. Instead of first infiltrating the porous PI film with PEO/LiTFSI, gold was sputtered onto both sizes of the porous PI thin film (Figure 9a). The advantage of this was threefold: first, it ensured the thickness was fixed at about 8.6 μm, and thus that the ionic conductivity measured was truly from the aligned channels; second, the rigid, flat surface of porous PI compared with PI/PEO/LiTFSI ensured the good adhesion and high continuity of the gold thin film; third, this process prevented the possible disruption of PEO/LiTFSI in the sputtering process and constrained the air exposure time of the composite electrolyte.

[0076] Shadow masks are used for the gold deposition, and the size of the deposited gold thin film is controlled to be about 0.4 cm × about 0.4 cm (Figure 9b). The size of the deposited gold thin film was smaller than the porous PI film to avoid shortage between the top and bottom surfaces at the film edge. The thickness of the gold film was controlled to be about 50nm (Figure 9c), and the adhesion between the deposited gold thin film and the PI substrate was strong. PEO/LiTFSI is then infiltrated into the channels, using the same method as the PI/PEO/LiTFSI followed with surface cleaning to avoid residual PEO/LiTFSI on the PI surface. The samples were then transferred into an Ar filled glovebox and heated on a hot plate at about 70 °C for more than about 48 h before EIS measurement.

[0077] Nyquist plots of a typical cell at about 20 °C, about 25 °C and about 30 °C are shown in Figure 10. For example, at about 25 °C, the resistance is about 344.9 Ohm. The ionic conductivity can be calculated from equation (1):

$$\sigma = \frac{d}{R \cdot A} \qquad (1)$$

where "d" is the distance between the two surfaces, "A" is the overlapping area of the conductor and "R" the resistance.

[0078] In the case here, the distance is about 8.6 μm, the area is about 0.16 cm^2, and the resistance at about 25 ºC is about 344.9 Ohm. From equation (1), the ionic conductivity of the calculated area is about 1.56×10^{-5} S/cm. Since the PEO/LiTFSI takes up about 11% of the area, the effective ionic conduction area is about 11% of the about 0.16 cm^2. As a result, the true ionic conductivity of PEO/LiTFSI in vertically aligned PI channels is about 1.4×10^{-4} S/cm at about 25 ºC. This matches the values of Figures 2e and 2f.

[0079] Nyquist plots of a typical cell with an electrode area of about 0.49 cm^2 (about 0.7 cm × about 0.7 cm) at about 20 ºC, about 25 ºC and about 30 ºC are also shown in Figure 11. These ionic conductivity values (from PEO/LiTFSI in nanochannels) are comparable to those measured with smaller area (about 0.16 cm^2) cells (about 1.2×10^{-4} S/cm at about 25 ºC). These result from a larger area test evidenced that the nanochannels of PI indeed enhances the ionic conductivity of PEO/LiTFSI.

[0080] Figures 12a and 12b shows the schematic of 2D-XRD with PEO/LiTFSI in vertical aligned channels in reflection mode. An EO:Li ratio of about 16:1 is used to ensure the existence of crystalline regions that could be identified with 2D-XRD. Schematic 2D-XRD patterns shown in Figures 12c and 12d (real patterns in Figure 12g and Figure 12h) are displayed by Figure 12b to rotate clockwise along x-axis at 90 degrees. The isotropic ring pattern in Figure 12c indicate the isotropic nature of PEO/LiTFSI film. However, the polarized 2D-XRD pattern in Figure 12d indicates the anisotropic nature of the PEO/LiTFSI confined in vertical aligned channels. In this case, the inner circle of the 2D-XRD ring concentrated along the y-axis reveals the crystallites are textured along the channels of the sample. The XRD analysis data of Figures 12g and 12h was obtained by integrating their pattern intensities, which is shown in Figures 12e and 12f. The PEO/LiTFSI film (Figure 12e) shows two sets of peaks, labelled with the dots and the triangles. Triangles at about 11.3º and about 14.6º indicate the existence of PEO_6LiTFSI complex crystallites, and the black dots at about 19.1º and about 23.3º indicate the formation of PEO crystallites. However, the

PEO/LiTFSI in vertical aligned channels (Figure 12f) shows the existence of just PEO crystallites (dots), which may also result from the nanoconfinement effect. The relative intensities of the about 19.1° and about 23.3° peaks in these two cases are different, also indicating the different crystallite textures in the two samples.

[0081] Li/SPE/Li symmetric cells cycled at about 0.1 mA/cm^2, about 40 °C are shown in Figure 14. Li/PI/PEO/LiTFSI/Li is stable for much longer than the Li/ PEO/LiTFSI /Li cells, given the superior mechanical properties of PI/PEO/LiTFSI.

[0082] In addition, the performance of Li/PI/PEO/LiTFSI/Li is tested at different current densities and areal capacities in an environmental chamber at about 60 °C (with high current densities and higher areal capacities). Note that in these tests the Li foil is coated with a very thin layer of PEO/LiTFSI/Al_2O_3 nanoparticles (about 2 μm, PEO:LiTISI:Al_2O_3=about 3:2:2 by weight) to improve the contact between Li and PI/PEO/LiTFSI (as shown in Figure 15a). Some residual PEO/LiTFSI may remain on the PI/PEO/LiTFSI solid electrolyte surface (due to the fabrication process) upon cell assembly. Cells were first activated by running five cycles at a low current density (about 0.05 mA/cm^2, about 0.025 mAh/cm^2). As shown in Figure 15b, Li/PI/PEO/LiTFSI/Li shows a very stable performance at various current densities and capacities (about 0.1 mA/cm^2, about 0.3 mAh, marked; about 0.2 mA/cm^2, about 0.5 mAh, marked; about 0.3 mA/cm^2, about 0.75 mAh, marked; about 0.4 mA/cm^2, about 1 mAh, marked) for about 400 h, and the zoomed-in images can be found in Figures 15c-15f. A control cell with just PEO/LiTFSI/Al_2O_3 coated Li metal (without PI/PEO/LiTFSI, Figure 15g) was also made. This symmetrical cell ran at exactly the same current density and capacity steps with the Li/PI/PEO/LiTFSI/Li cell until about 200 h. The control cell shorted in about 5 h at a low current density (about 0.05 mA/cm^2, about 0.025 mAh, Figures 15h and 15i), which proves that the PEO/LiTFSI/Al_2O_3 coating will not prevent the two Li metals from short circuiting upon cycling, and the stable performance of the Li/PI/PEO/LiTFSI/Li cell resulted from the protection of PI/PEO/LiTFSI.

[0083] The cell is further cycled at about 0.5 mA/cm^2, about 1.5 mAh for another about 500 h (Figure 16a), which continuously demonstrated its stable cycling performance. Figure 16b and Figure 16c also provide the zoomed in view of one Li plating/stripping cycle at around the 500th and 800th hour.

[0084] To determine the thickness of the PEO/LiTFSI/Al_2O_3 nanoparticle film on Li metal, a focused-ion-beam (FIB) characterization is applied to the Li/PEO/LiTFSI/Al_2O_3 sample. The preparation of the Li/PEO/LiTFSI/Al_2O_3 sample was the same as for the Li/PI/PEO/LiTFSI/Li cell, except the PEO/LiTFSI/Al_2O_3 was supported by a PTFE thin film so that it was readily peeled off for FIB characterization (Li foil was first scratched to remove surface contamination so that pure Li could be exposed in the glovebox before applying the coating film). The Li/PEO/LiTFSI/Al_2O_3 sample was loaded on an SEM stage and sealed tightly with Aluminum pouch bags in the Ar filled glovebox before loading into the FIB. The FIB used was a FEI Helios NanoLab 600i DualBeam FIB/SEM. The Li/PEO/LiTFSI/Al_2O_3 was exposed to air for less than about 3 seconds before being transferred into the FIB chamber.

[0085] As shown in Figure 17a, an about 50 μm×50 μm×30 μm opening was cut by FIB into the sample (Li/PEO/LiTFSI/Al_2O_3 surface, top view). The zoomed-in image (tilted view) in Figure 17b shows the edge of Li/PEO/LiTFSI/Al_2O_3. A further zoom in (from the box in Figure 17) shows the cross-sectional image (tilted view) of the Li/PEO/LiTFSI/Al_2O_3 sample near the surface (Figure 17c). The 3D structure of Figure 17c's region is illustrated in Figure 17d to identify the thickness of the PEO/LiTFSI/Al_2O_3 layer. In Figure 17c and Figure 17d, the light shading stands for the top surface of the PEO/LiTFSI/Al_2O_3 layer, the dark shading stands for the cross-sectional image of the PEO/LiTFSI/Al_2O_3 layer (where the Al_2O_3 particles with diameters of about 50 nm can be identified), and the grey shading stands for the cross section of bulk lithium. The thickness of the PEO/LiTFSI/Al_2O_3 layer is identified to be about 2 μm (corrected length with tilted angle).

[0086] To supplement the electrochemical test results, the Li/PI/PEO/LiTFSI/Li symmetrical cell is disassembled after cycling. For the purpose of further characterization, the PI/PEO/LiTFSI film was peeled off of the cell and cleaned with acetonitrile to wash away the residual polymer electrolyte on PI. The SEM images of pristine PI (Figure 18a) are taken from Figure 2a and Figure 8a for direct comparison with the cycled PI film (Figures 18c and 18d). From the SEM images, no noticeable difference can be found between the pristine film and the cycled film at different magnifications. No noticeable cleavage or rupture of channels is found. This phenomenon indicates that in a stable cell, the Li deposition does not damage the channels in the PI film. A number of SEM images (at different magnifications) with intact surface structure of the PI film after cycling are also displayed in Figure 19.

[0087] To understand why the deposition of Li does not penetrate through the "soft" channel region of this high modulus matrix/high ionic conductivity (soft) filler structure, theoretical calculations are performed in two stages. Theoretical simulations are carried out to understand the distribution of current density and lithium ions in the battery. The parameters of the model are set to be identical to the real coin cells; details of the model can be found in the method part toward the end of the present disclosure. Figure 20a shows the schematic image and dimensions of the model system. The gray channels in between two PEO/Al_2O_3 buffer layers are the Li ion conducting channels in the porous PI film, where the Li ion concentration is 3 mol/L. A 0.4 mA/cm^2 current density is then applied through the sandwich structure. At steady state (time = 100s), the Li ion concentration changed, but the variation is very constrained (0.02 mol/L difference from top to bottom). This means the high ionic conductivity of PEO in the channels is sufficient to support the current density of 0.4 mA/cm^2, such that no Li ion depletion or severe concentration gradient would occur at these conditions.

[0088] The current density distribution is also calculated through the above model. As shown in Figure 21a, current density soon became uniform at 0.4 mA/cm^2 after passing the channels. The current density taken at 1 μm deep shows a very flat line at 0.4 mA/cm^2 (Figure 21b). Even when the PEO/Al_2O_3 layer decreases to 0.3 μm as more Li is deposited (Figure 21c), very constrained current fluctuations occur at the electrode surface (Figure 21d). Thus, at this stage, the non-depleted, uniform current density will tend towards a uniform Li deposition at the electrode surface, instead of forming dendritic Li at initial lithium plating stages. Nevertheless, when the deposition front is very close (e.g. < 300 nm) to the nanochannel, current non-uniformity increases.

[0089] To understand the possibly non-uniform lithium deposition behavior when the Li deposition front is very close (< 300 nm) to the nanochannel, a phase-field simulation of the lithium deposition process is applied (The parameters of the modeling are set to be identical to the real coin cells and details of the modeling can be found in the method part toward the end of the present disclosure). The phase-field simulation computationally reproduced the processes of multiphase morphology evolution (Figures 22a-f), Li ion concentration redistribution (Figures 22g-l) and electrostatic overpotential variation (Figures 22m-r) during Li plating, starting from a pristine Li metal anode surface in the solid electrolyte half-cell. At the initial stages (Figures 22a-c), the flat Li metal surface protrudes towards the Li-ion

conductive PEO channel due to the locally elevated Li ion flux. After contact with solid electrolyte (Figures 22c-f), the Li metal protrusion growth (in Y direction) is slowed down and gradually dominated by the lateral growth (in X direction) along the deformed electrolyte surface (Figure 22f).

[0090] From the simulated morphologies demonstrated above, the PEO-filled nanochannels are not penetrated by Li deposits. This is further validated by an analysis of the driving force contribution at the channel region over plating time (Figure 23). The morphological evolution process involves competition between surface/interface, mechanical and electrochemical energies; just the electrochemical part contributes positively to the growth of Li metal phase. In this nanoscale system of evaluation, the surface/interface energy contribution maintains a notably high percentage (about 40% in average) of the total throughout the entire process. When elastic deformation occurs after around 200 s (Figure 22c), the negative contribution from the surface/interface and mechanical driving forces begins to increase prominently. At around 270 s, the contribution of electrochemical driving force decreases below about 50%, and thus can no longer overcome the interfacial and elastic energy barrier to nucleate Li nano-dendrites into the channel. Therefore, the deposited Li metal tends to push toward the electrolyte phase as a whole rather than penetrating through the nanochannel.

[0091] To validate the hypothesis, fabrication is made of Li/PI/PEO/LiTFSI/Cu (about 2 μm PEO/Al_2O_3 on both Li and Cu surface) coin cells with about 0.4 mA/cm^2, about 1 mAh/cm^2 Li deposition (same Li plating condition of liquid electrolyte in Figure 3c). Cu is chosen instead of Li because Cu has a very flat surface, making it convenient to observe and determine the deposited Li morphology. After Li deposition, the coin cells are disassembled and the Li deposited Cu foil is taken out for further characterization. As shown in Figure 24a, the surface under PI/PEO/LiTFSI has many cone-like protrusions. Statistics on the size of these cone-like protrusions (Figure 24b) shows that most of them are in the range of about 2-3 μm, with a few even larger than about 4 μm. It is also noticeable that none of them have sizes that are smaller than about 1 μm. This indicates that the deposition of Li follows the phase field modeling prediction, in which deposited Li metal tends to form large cone-like protrusions and push toward the electrolyte phase as a whole rather than penetrating through the channel.

[0092] FIB was then applied to open the cone-like protrusions and validate that these are deposited Li instead of polymer electrolyte protrusions left behind by an incomplete removal process. A pristine protrusion is shown in Figure 25a. After the FIB (Figure 25b) was applied, its cross section shows a distinct contrast between the inner material and surface material. This can also be observed in other protrusions as shown in Figure 25c and Figures 25e-f. SEM images in backscattered electron (BSE) mode are displayed in Figure 25d (normal secondary electron counterpart image shown in Figure 25c), which also shows the core-shell structure. The darker colored core can be identified as deposited Li and the lighter color shell as the solid (Lithium)-solid (solid electrolyte) interface and residual PEO/Al_2O_3.

[0093] From the above discussions, it is concluded that at normal battery operation conditions, the deposited Li will not tend to grow into the soft channel region, validating the effectiveness of the soft-vertical-nanochannel/hard-matrix SPE structures. According to the phase field simulation, such phenomenon can be understood as the electrochemical driving force being unable to overcome the interfacial and elastic energy barrier to nucleate Li nano-dendrites into the channel.

[0094] Figure 26 displays the stable cycling performance of Li/PI/PEO/LiTFSI/LFP at C/5. Voltage profile of Li/PI/PEO/LiTFSI/LFP at C/5, about 40 ºC is shown in Figure 27 (LFP loading of about 1.5 mg/cm^2, areal capacity of about 0.2 mAh/cm^2).

[0095] Figure 28 displays the cycling performance of Li/PI/PEO/LiTFSI/LFP at C/10 (LFP loading of about 1.5 mg/cm^2, areal capacity of about 0.2 mAh/cm^2). Voltage profile of Li/PI/PEO/LiTFSI/LFP at C/10, about 30 ºC is shown in Figure 28a. Cycling performance of the Li/PI/PEO/LiTFSI/LFP at C/10 about 30 ºC is shown in Figure 28b. The slight increase of specific capacity with cycle may result from the "activation" of battery materials. The fact that Li/PI/PEO/LiTFSI/LFP can be stable cycled at low temperatures such as about 40 ºC and about 30 ºC indicates PI/PEO/LiTFSI as a promising polymer-polymer composite SSE.

[0096] To further demonstrate the compatibility of our solid electrolyte under high cathode loading conditions, batteries with PI/PEO_{10k}/LiTFSI electrolytes are tested with different cathode loading at about 40 ºC. As shown in Figure 29a, the areal capacity of LFP/PI/PEO/$LiTFSI_{10}$/Li cells can achieve stable cycling performance of about 0.91 mAh/cm^2 and about 0.47 mAh/cm^2 with LFP loadings of about 6.9 mg/cm^2 and about 3.9 mg/cm^2, respectively. Voltage profiles of these batteries are shown in Figure 29b and Figure

29c. These demonstrate that the PI/PEO/LiTFSI composite electrolyte system is compatible with high cathode loading near ambient conditions.

[0097] ***Current redistribution modeling*** Models were created using COMSOL Multiphysics with a 2D model and the physical module "Tertiary Current Distribution, Nernst-Planck". The current density supplied by the Li counter electrode was set to 0.4 mA/cm^2. The diffusion coefficient of Li was set to $3.48x10^{-7}$ cm^2/s for PEO/LiTFSI in the pores and $8.93x10^{-8}$ cm^2/s for PEO/LiTFSI/Al_2O_3. The pore diameter was set to 200 nm, corresponding to the size of the track- etched pores. The spacing between the pores was set as 375 nm, corresponding to a PI membrane porosity of 11%, assuming a hexagonally close-packed pore array. Initial concentration of Li in the solid electrolyte was set to 3 M, corresponding to an EO:Li ratio of 10:1. A 2 μm thick layer of PEO/LiTFSI/Al_2O_3 was placed on the counter Li electrode.

[0098] The steady state current distribution was found by applying the current density for 100 s. The results were confirmed to be steady state by making sure the current and concentration profiles did not change over 10s of seconds.

[0099] ***Li deposition Phase Field modeling*** A multiphase-field model incorporating elasticity and nonlinear Butler-Volmer kinetics was developed for Li electrodeposition in a polymer composite solid electrolyte half-cell system. Two phase-field order parameters, ξ and ϕ, were introduced to describe the relative mass density of different phases: $\{\xi = 1; \phi = 0\}$ for Li metal, $\{\xi = 0; \phi = 1\}$ for solid electrolyte and $\{\xi = 0; \phi = 0\}$ for the PEO interlayer in between the anode and electrolyte. The phase-fields vary continuously between 1 and 0 with a finite thickness of diffuse interfaces at phase boundaries. Due to the interfacial affinity, the PI-PEO composite electrolyte is treated as one phase-field mathematically, but defined with different moduli and Li ion conductivities. Given the 4~5 order of magnitude difference in elastic modulus between PEO and PI/Li metal, the PEO interlayer resistance to Li deposit growth is assumed small enough. The total free energy of the system, including chemical, interfacial, electrostatic and mechanical contributions, is written as

$$G = \int \left[f_{chem}(\tilde{c}) + f_{intf}(\tilde{c}) + f_{elec}(\tilde{c}, \varphi) + f_{mech}(\tilde{c}) \right] dV$$

$\tilde{c}$ is a set of dimensionless densities/concentrations

$\tilde{c} = \{\rho_{Li}/\rho_0^{Li} = \xi, \rho_{SE}/\rho_0^{PI-PEO} = \phi, c_{Li+}/\ c_0 = \tilde{c}_+\}$, where ρ_0^{Li}, ρ_0^{PI-PEO} and c_0 are the mass density of Li metal, PI-PEO composite, and the Li ion bulk concentration of solid electrolyte, respectively.

$f_{chem} = f_0(\xi, \phi) + c_0 RT \sum_i \tilde{c}_i \ln \tilde{c}_i + \sum_i c_i \mu_i^{\ominus}$ is the bulk energy density in the standard reference state (Θ), where the local free energy density $f_0(\xi, \phi) = A\phi^2(1-\phi)^2 + B\xi^2(1-\xi)^2 + (c/2)\,\phi^2\xi^2$ consists of two double-well functions and a cross term. The phenomenological parameters are set to be $A = B = 1/4C = 1$, such that f_0 has degenerate minima representing each phase with equal depth located at equilibrium states. The interfacial energy density takes the form of $f_{intf} = \frac{1}{2}\kappa_\xi (\nabla\xi)^2 + \frac{1}{2}\kappa_\phi (\nabla\phi)^2$, where κ_ξ and κ_ϕ are gradient energy coefficients associated with the surface/interface energies of Li metal and solid electrolyte. The Li dendrite growth anisotropy is described by the gradient energy coefficient κ_ξ, in the form of $\kappa_\xi(\theta) = \kappa_{Li}[1 + \delta\cos(\omega\theta)]$, where κ_{Li} is related to the Li metal surface energy, δ and ω are the strength and mode of the anisotropy, and θ is the angle between the normal vector of the local interface and the reference axis. The electrolyte is assumed isotropic and thus κ_ϕ is constant.

$f_{elec}(\vec{c}, \varphi) = F\sum_i z_i c_i \varphi$ is the electrostatic energy density, where F is Faraday constant, φ is electrostatic potential, and z_i is the valence of charged species. The elastic energy density is written as:

$f_{mech} = \frac{1}{2} C_{ijkl}\varepsilon_{kl}\varepsilon_{ij}$, where the stiffness

$C_{ijkl} = \left[h(\xi)E_{ijkl}^{\xi} + \sum h(\phi_i)E_{ijkl}^{\phi}\right]$ is expressed in term of interpolating function

$h(\xi) = \xi^3(10 - 15\xi + 6\xi^2)$ and the elasticity tensors of Li metal (E_{ijkl}^{ξ}) and electrolyte (E_{ijkl}^{ϕ}). Considering the random orientation of Li metal/electrolyte interfaces, we incorporated the isotropic case of elasticity. Therefore, the phase morphology evolution equation for the Li metal phase is governed by the Butler-Volmer kinetics coupled Allen-Cahn equation

$$\frac{\partial \xi}{\partial t} = -L_{\sigma}^{\xi}\left\{\frac{\partial f_0}{\partial \xi} - \kappa_{\xi}\nabla^2\xi + \frac{\partial f_{mech}}{\partial \xi}\right\} - L_{\eta}^{\xi}h'(\xi)\left[-\tilde{c}_{+}\, exp\frac{-\alpha F\eta}{RT} + exp\frac{(1-\alpha)F\eta}{RT}\right]$$

where L_{σ}^{ξ} and L_{η}^{ξ} are interface mobility and reaction constant, respectively. α is the Butler-Volmer symmetric factor and η is the overpotential. Likewise, the evolution equation for electrolyte phase is:

$$\frac{\partial \phi}{\partial t} = -M_{\phi}\left\{\frac{\partial f_0}{\partial \phi} - \kappa_{\phi}\nabla^2\phi + \frac{\partial f_{mech}}{\partial \phi}\right\}$$

where M_{ϕ} is the interface mobility of solid electrolyte. The evolution of each phase-field was solved simultaneously with Li ion diffusion, charge conservation and mechanical equilibrium equations. The model details and parameter table are in references, e.g., Tian, H. K., et al. Computational study of lithium nucleation tendency in $Li_7La_3Zr_2O_{12}$ (LLZO) and rational design of interlayer materials to prevent lithium dendrites. *Journal of Power Sources* (2018); Hongahally Basappa, R. *et al.* Grain boundary modification to suppress lithium penetration through garnet-type solid electrolyte. *Journal of Power Sources* (2017); Yang, C. *et al.* An Electron/Ion Dual-Conductive Alloy Framework for High-Rate and High-Capacity Solid-State Lithium-Metal Batteries. *Advanced Materials* (2018).

[0100] All phase-field simulations were performed in a $4 \times 4\ \mu m$ half-cell system, meshed by a 200×200 grid, using COMSOL Multiphysics 5.2. Major simulation parameters are set to be consistent with the available experimental data. The diameter of the PEO channel and the thickness of the PEO interlayer are both $200\ nm$. The Li ion conductivities in channel, interlayer and PI are $10^{\mathrm{Hs}}\ S/cm$, $3 \times 10^{\mathrm{HY}}\ S/cm$ and 0, respectively. The elastic modulus of Li metal, PI and PEO are $4.9GPa$, $850MPa$ and $1MPa$, respectively. Excluding the negligible impact of SEI layer (Tsai, C. L. *et al.* $Li_7La_3Zr_2O_{12}$ Interface Modification for Li Dendrite Prevention. *ACS Applied Materials and Interfaces* (2016)), the surface energies of Li metal and solid electrolyte used in this simulation are $0.48\ J/m^{\mathrm{T}}$ and $0.05\ J/m^{\mathrm{T}}$, respectively. An implicit time integration was used with timestep of $0.2\ s$. Li plates at a constant overpotential of $0.1\ V$ for $340\ s$, with an average current density of $0.3\ mA/cm^{\mathrm{T}}$. A Dirichlet boundary condition was applied for electrolyte bulk concentration ($c_{\mathrm{C}} = 3\ mol/L$) on the boundary. No noise terms were included in the simulations.

Table 1. Energy density calculation of different solid-state electrolyte systems

#	Solid electrolytes	Thickness (μm)	Density (g/cm³)	Areal density of SSE (mg/cm²)	Energy density (Wh/kg)
C	**PI/PEO/LiTFSI**	**8.6**	**1.4**	**1.2**	**244.4**
D1	LLZO (25wt%) /PEO/LiTFSI	45	*1.67	7.5	142.7
D2	LLZO(40wt%) /PEO/LiTFSI	35	*1.93	6.8	150.5
D3	PEO/LiTFSI SiO_2	200	1.5	30.0	57.7
E1	LLZO (ultrathin)	15	5	7.5	147.9
E2	LGPS	240	2.94	70.6	28.0
E3	LLZO	200	5	100.0	20.2

[0101] As used herein, the singular terms "a," "an," and "the" may include plural referents unless the context clearly dictates otherwise. Thus, for example, reference to an object may include multiple objects unless the context clearly dictates otherwise.

[0102] As used herein, the terms "substantially," "substantial," and "about" are used to describe and account for small variations. When used in conjunction with an event or circumstance, the terms can refer to instances in which the event or circumstance occurs precisely as well as instances in which the event or circumstance occurs to a close approximation. When used in conjunction with a numerical value, the terms refer to a range of variation of less than or equal to ±10% of that numerical value, such as less than or equal to ±5%, less than or equal to ±4%, less than or equal to ±3%, less than or equal to ±2%, less than or equal to ±1%, less than or equal to ±0.5%, less than or equal to ±0.1%, or less than or equal to ±0.05%.

[0103] As used herein, the term "size" refers to a characteristic dimension of an object. Thus, for example, a size of an object that is circular can refer to a diameter of the object. In the case of an object that is non-circular, a size of the non-circular object can refer to a diameter of a corresponding circular object, where the corresponding circular object exhibits or has a particular set of derivable or measurable characteristics that are substantially the same as those of the non-circular object. When referring to a set of objects as having a particular size,

it is contemplated that the objects can have a distribution of sizes around the particular size. Thus, as used herein, a size of a set of objects can refer to a typical size of a distribution of sizes, such as an average size, a median size, or a peak size.

[0104] Additionally, amounts, ratios, and other numerical values are sometimes presented herein in a range format. It is to be understood that such range format is used for convenience and brevity and should be understood flexibly to include numerical values explicitly specified as limits of a range, but also to include all individual numerical values or sub-ranges encompassed within that range as if each numerical value and sub-range is explicitly specified. For example, a ratio in the range of about 1 to about 200 should be understood to include the explicitly recited limits of about 1 and about 200, but also to include individual ratios such as about 2, about 3, and about 4, and sub-ranges such as about 10 to about 50, about 20 to about 100, and so forth.

[0105] While the disclosure has been described with reference to the specific embodiments thereof, it should be understood by those skilled in the art that various changes may be made and equivalents may be substituted without departing from the true spirit and scope of the disclosure as defined by the appended claim(s). In addition, many modifications may be made to adapt a particular situation, material, composition of matter, method, operation or operations, to the objective, spirit and scope of the disclosure. All such modifications are intended to be within the scope of the claim(s) appended hereto. In particular, while certain methods may have been described with reference to particular operations performed in a particular order, it will be understood that these operations may be combined, sub-divided, or re-ordered to form an equivalent method without departing from the teachings of the disclosure. Accordingly, unless specifically indicated herein, the order and grouping of the operations is not a limitation of the disclosure.

[0106] All publications, patent applications, issued patents, and other documents referred to in this specification are herein incorporated by reference as if each individual publication, patent application, issued patent, or other document was specifically and individually indicated to be incorporated by reference in its entirety. Definitions that are contained in text incorporated by reference are excluded to the extent that they contradict definitions in this disclosure.

[0107] Other embodiments are set forth in the following claims.

What is claimed is:

1. A composite solid electrolyte, comprising:

a porous matrix having channels; and

ionically conducting fillers disposed within the channels.

2. The composite solid electrolyte of claim 1, wherein the porous matrix is a porous polymeric matrix.

3. The composite solid electrolyte of claim 2, wherein the porous polymeric matrix is a porous polymeric film.

4. The composite solid electrolyte of claim 3, wherein the porous polymeric film has a first major surface and an opposite, second major surface, and the channels extend at least partially through a thickness of the porous polymeric film between the first surface and the second surface.

5. The composite solid electrolyte of claim 4, wherein at least some of the channels extend fully through the thickness of the porous polymeric film between the first surface and the second surface.

6. The composite solid electrolyte of claim 4, wherein an alignment direction is specified as orthogonal to the first surface or the second surface, and at least some of the channels extend between the first surface and the second surface along respective longitudinally extending directions that are within ±35° of the alignment direction.

7. The composite solid electrolyte of claim 4, wherein the thickness of the porous polymeric film is about 100 μm or less.

8. The composite solid electrolyte of claim 1, wherein the porous matrix has an elastic modulus of about 10 MPa or greater.

9. The composite solid electrolyte of claim 1, wherein the channels have lateral dimensions in a range of about 1 nm to about 1000 nm.

10. The composite solid electrolyte of claim 1, wherein the ionically conducting fillers include a solid polymer electrolyte.

11. The composite solid electrolyte of claim 10, wherein the solid polymer electrolyte includes a polymer and a lithium-containing salt.

12. The composite solid electrolyte of claim 11, wherein the polymer is a polyether.

13. A solid-state lithium battery, comprising:

a cathode;

an anode; and

the composite solid electrolyte of any of claims 1-12 disposed between the cathode and the anode.

14. The solid-state lithium battery of claim 13, wherein the anode is a metallic lithium anode.

15. A manufacturing method of a composite solid electrolyte, comprising:

providing a porous matrix having channels;

infusing a solution of a polymer and a lithium-containing salt into the channels of the porous matrix; and

heating the infused porous matrix to form the composite solid electrolyte.

FIGURE 1

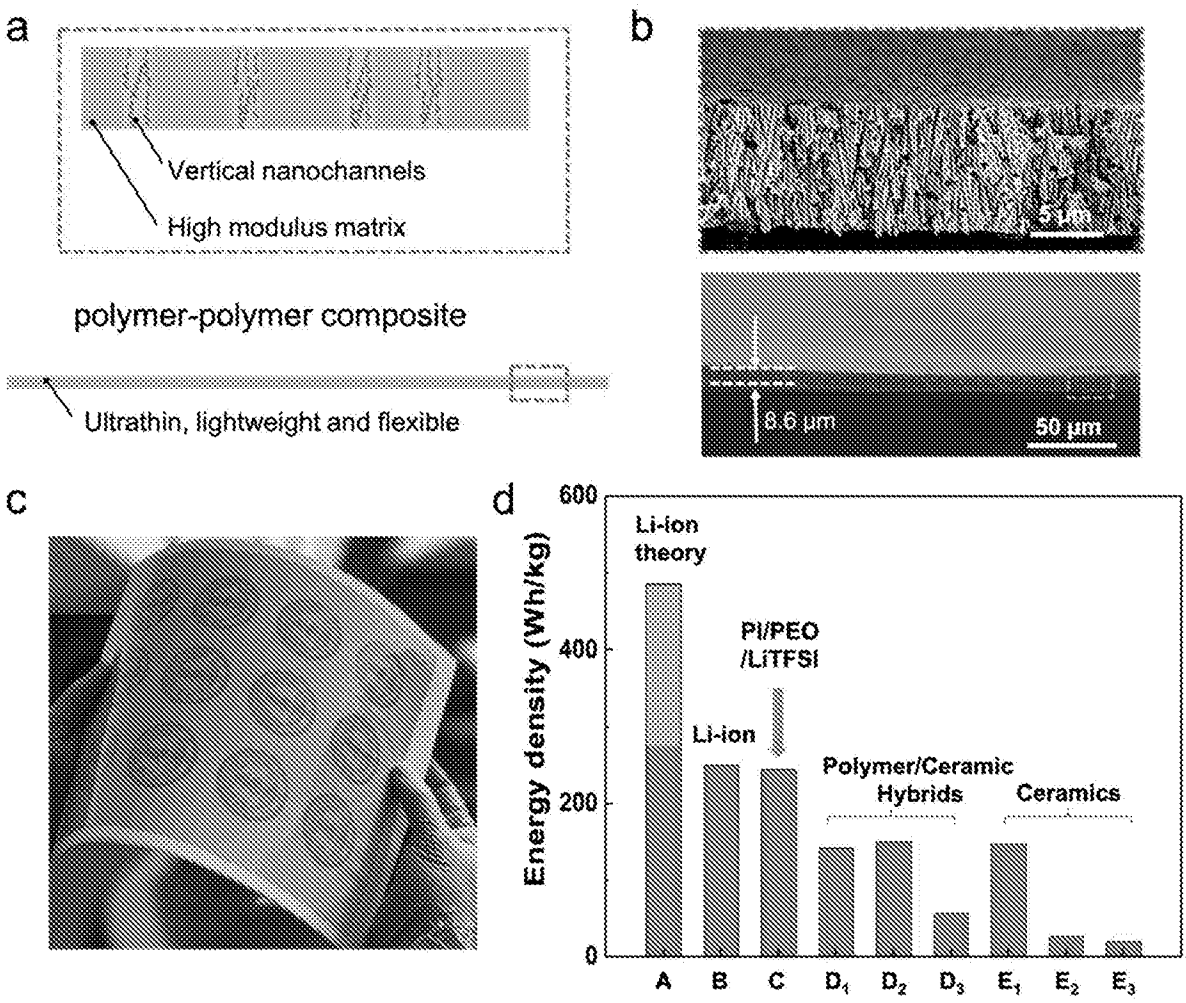
a
Vertical nanochannels
High modulus matrix
polymer-polymer composite
Ultrathin, lightweight and flexible
b
5 µm
8.6 µm
50 µm
c
d
Energy density (Wh/kg)
600
400
200
0
Li-ion theory
PI/PEO /LiTFSI
Li-ion
Polymer/Ceramic Hybrids
Ceramics
A
B
C
D1
D2
D3
E1
E2
E3

FIGURE 2

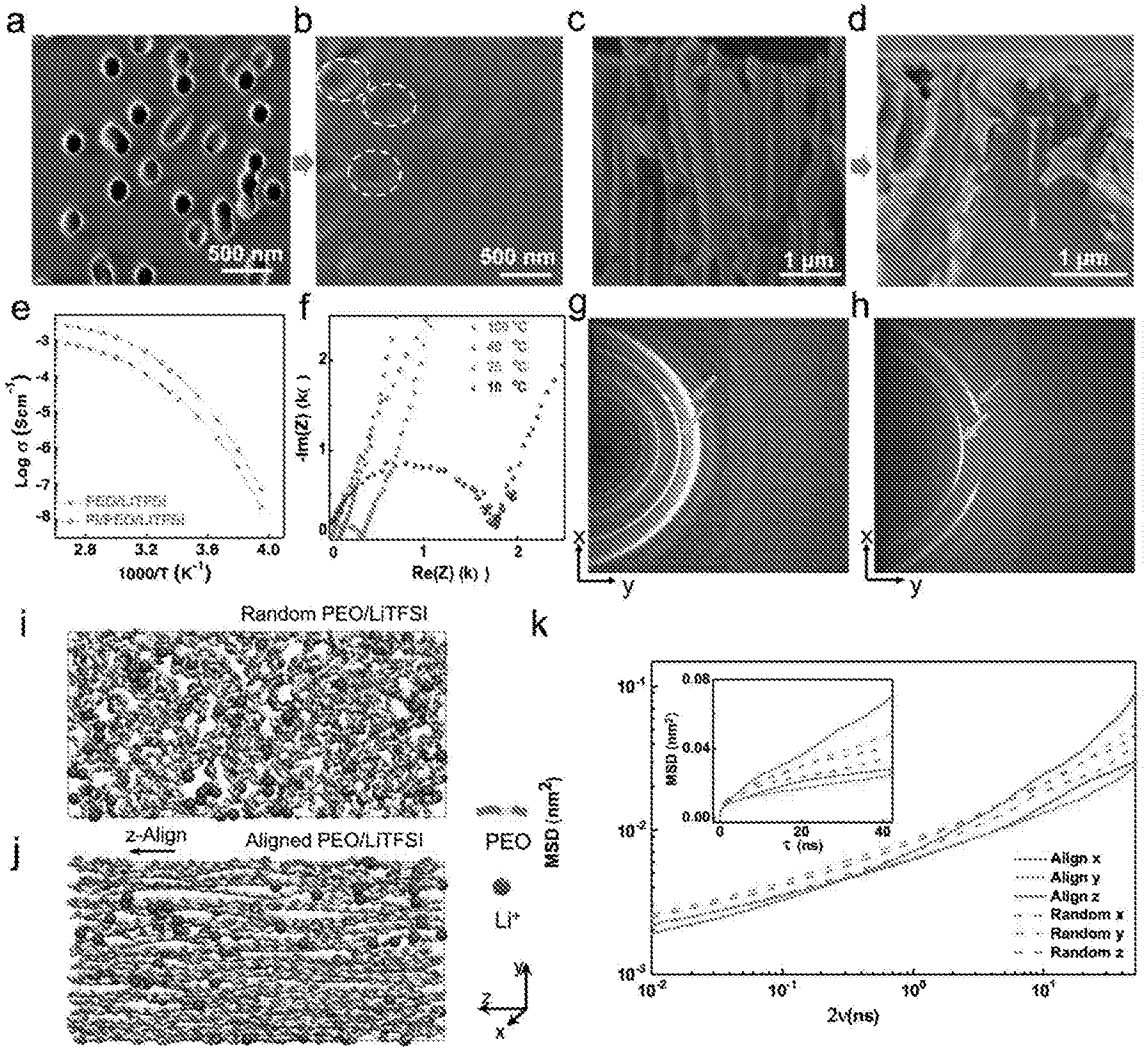
a
b
c
d
500 nm
500 nm
1 μm
1 μm
e
f
g
h
Log σ (Scm⁻¹)
1000/T (K⁻¹)
-Im(Z) (kΩ)
Re(Z) (kΩ)
x
y
i
Random PEO/LiTFSI
j
z-Align
Aligned PEO/LiTFSI
PEO
Li⁺
k
MSD (nm²)
τ (ns)
2τ(ns)
Align x
Align y
Align z
Random x
Random y
Random z

FIGURE 3

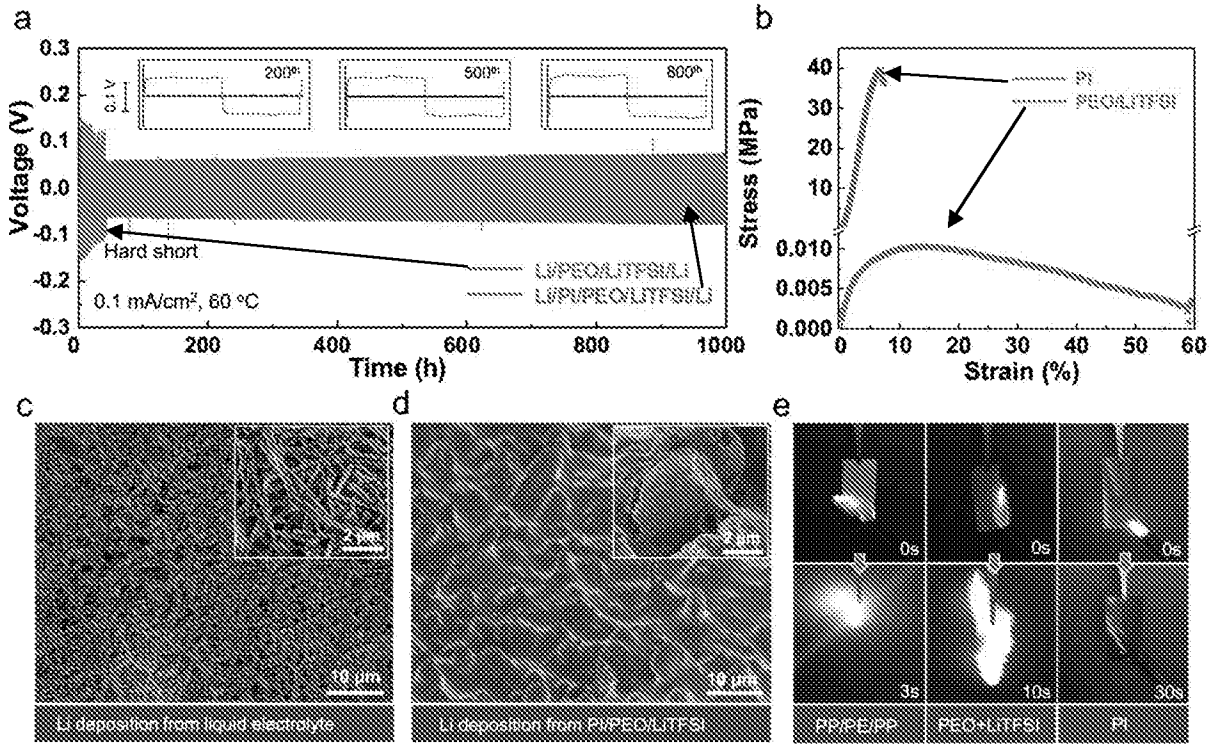
a
Voltage (V)
Time (h)
Hard short
0.1 mA/cm², 60 °C
Li/PEO/LiTFSI/Li
Li/PI/PEO/LiTFSI/Li
200th
500th
800th
b
Stress (MPa)
Strain (%)
PI
PEO/LiTFSI
c
d
e
10 μm
Li deposition from liquid electrolyte
Li deposition from PI/PEO/LiTFSI
PP/PE/PP
PEO+LiTFSI
PI
0s
3s
10s
30s

FIGURE 4

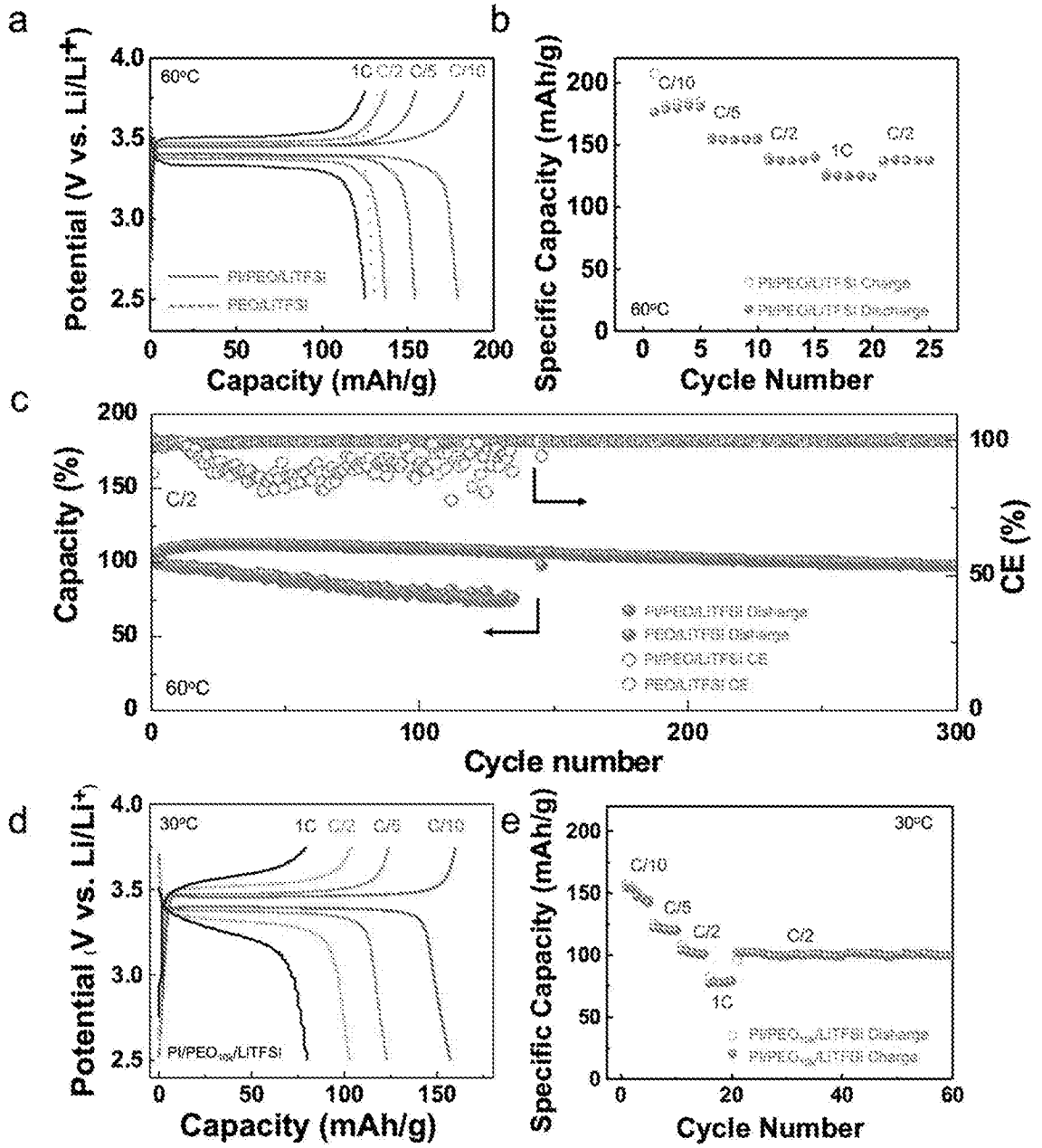
a
Potential (V vs. Li/Li+)
Capacity (mAh/g)
60°C
1C C/2 C/5 C/10
PI/PEO/LITFSI
PEO/LITFSI
b
Specific Capacity (mAh/g)
Cycle Number
C/10
C/5
C/2
1C
C/2
60°C
PI/PEO/LITFSI Charge
PI/PEO/LITFSI Discharge
c
Capacity (%)
CE (%)
Cycle number
C/2
60°C
PI/PEO/LITFSI Discharge
PEO/LITFSI Discharge
PI/PEO/LITFSI CE
PEO/LITFSI CE
d
Potential (V vs. Li/Li+)
Capacity (mAh/g)
30°C
1C C/2 C/5 C/10
PI/PEO20/LITFSI
e
Specific Capacity (mAh/g)
Cycle Number
30°C
C/10
C/5
C/2
C/2
1C
PI/PEO20/LITFSI Discharge
PI/PEO20/LITFSI Charge

FIGURE 5

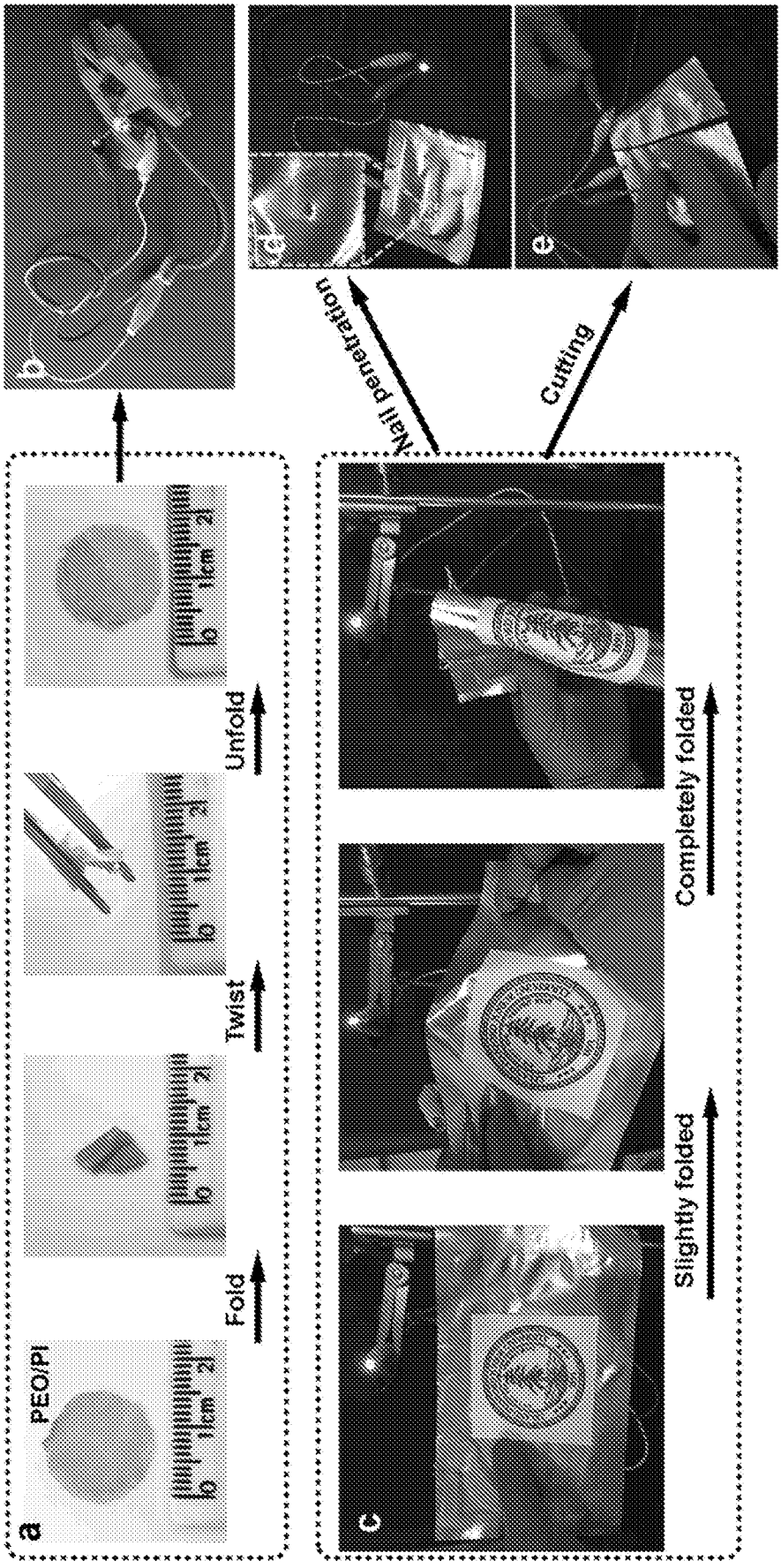
a
PEO/PI
Fold
Twist
Unfold
b
d
e
Nail penetration
Cutting
c
Slightly folded
Completely folded

FIGURE 6

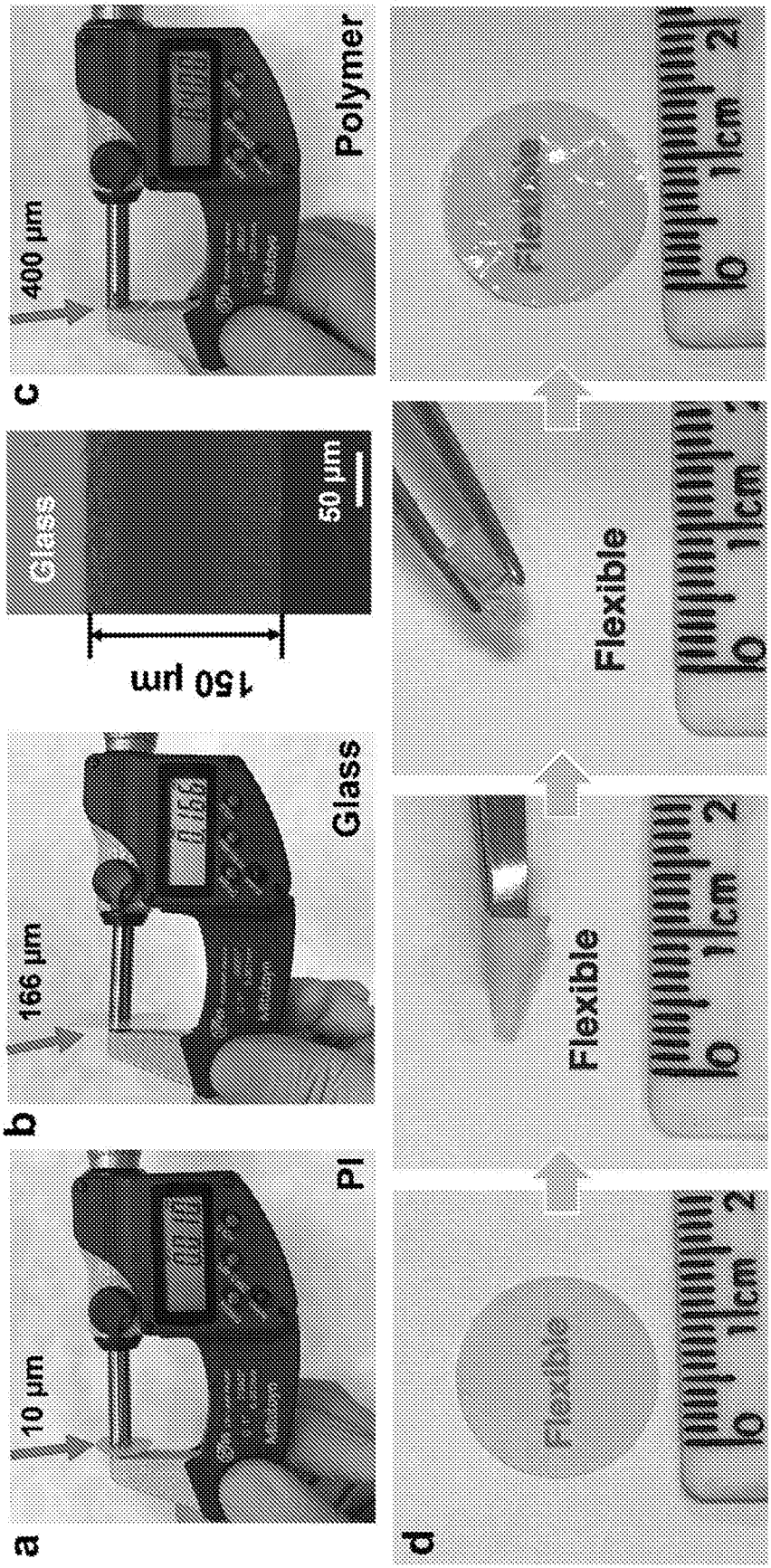
a
10 µm
PI
b
166 µm
Glass
150 µm
Glass
50 µm
c
400 µm
Polymer
d
Flexible
Flexible

FIGURE 7

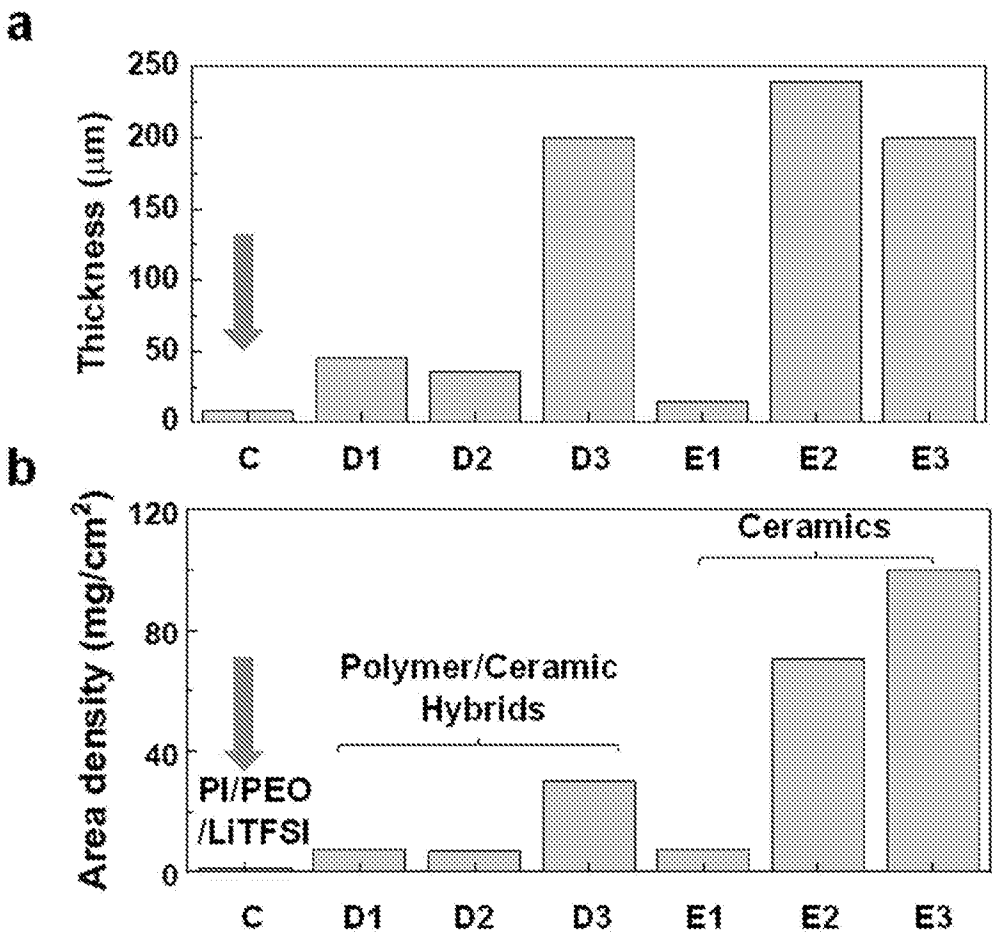
a
Thickness (μm)
250
200
150
100
50
0
C
D1
D2
D3
E1
E2
E3
b
Area density (mg/cm²)
120
80
40
0
Ceramics
Polymer/Ceramic Hybrids
PI/PEO /LiTFSI
C
D1
D2
D3
E1
E2
E3

FIGURE 8

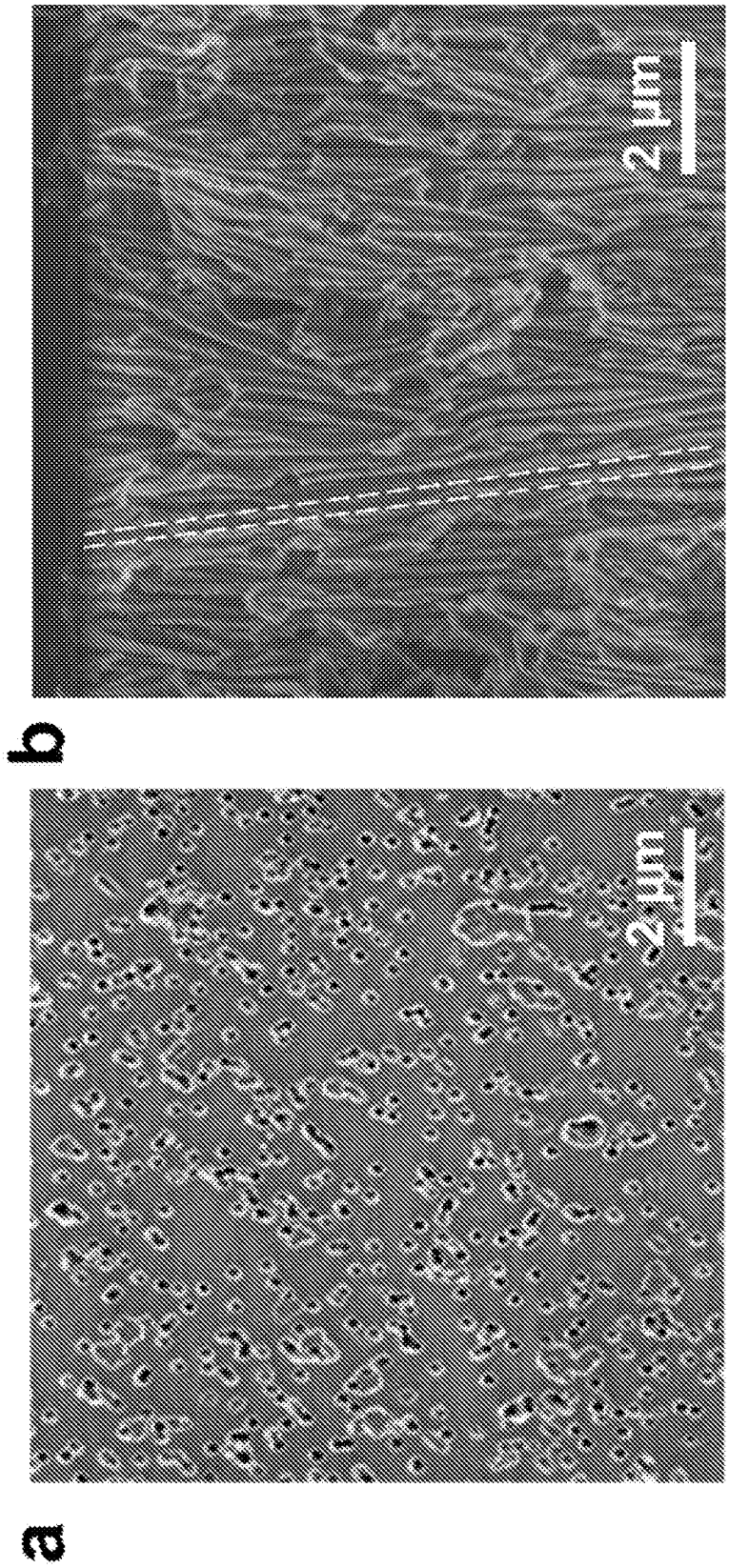

FIGURE 9

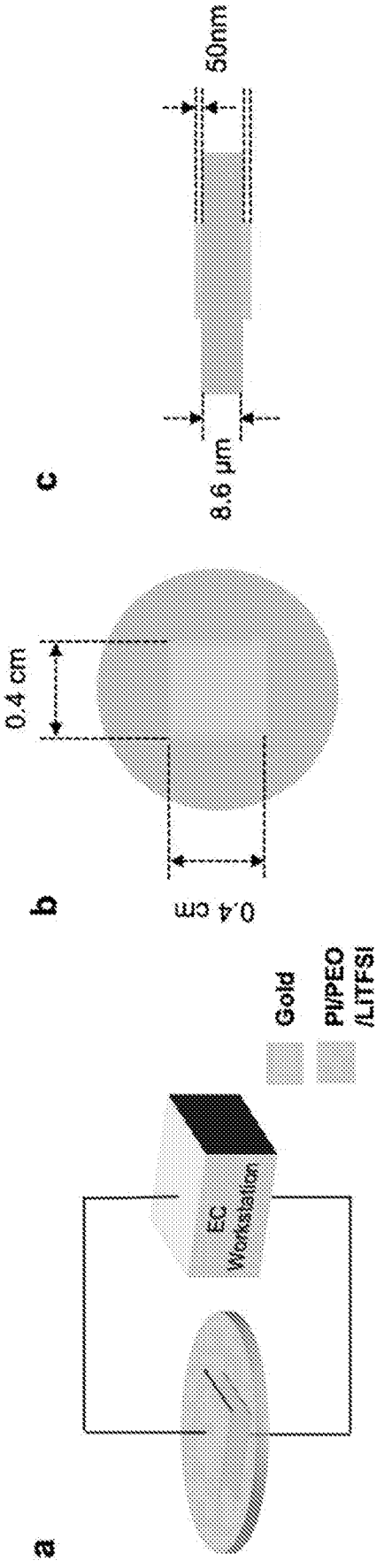

FIGURE 10

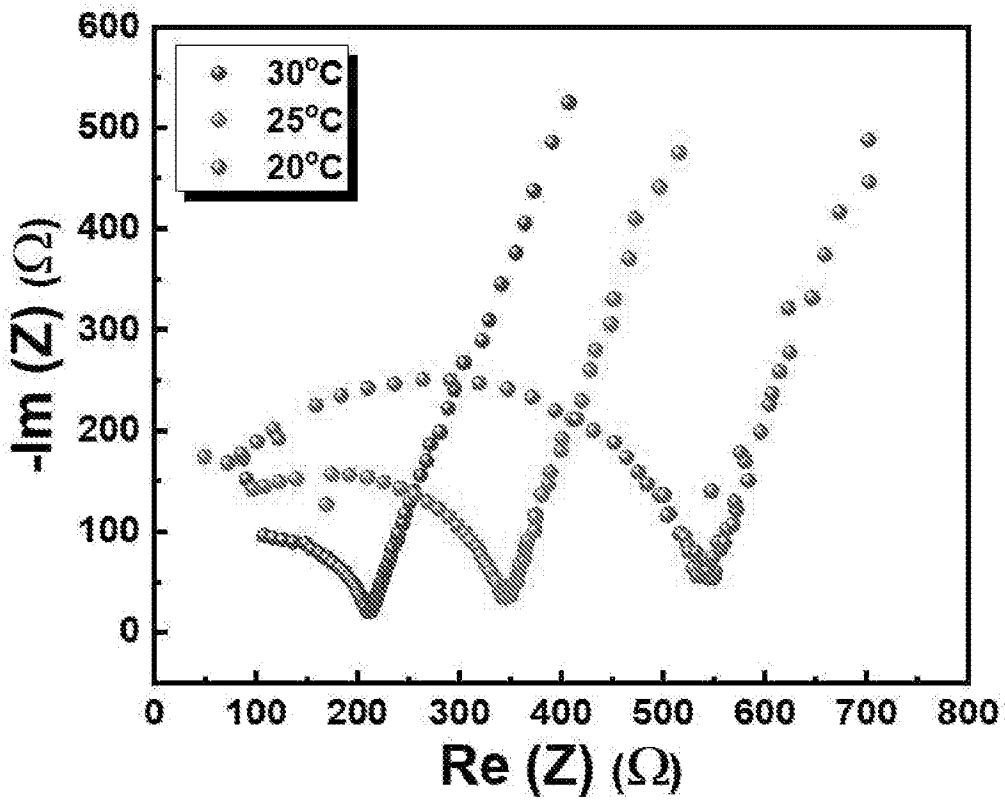

FIGURE 11

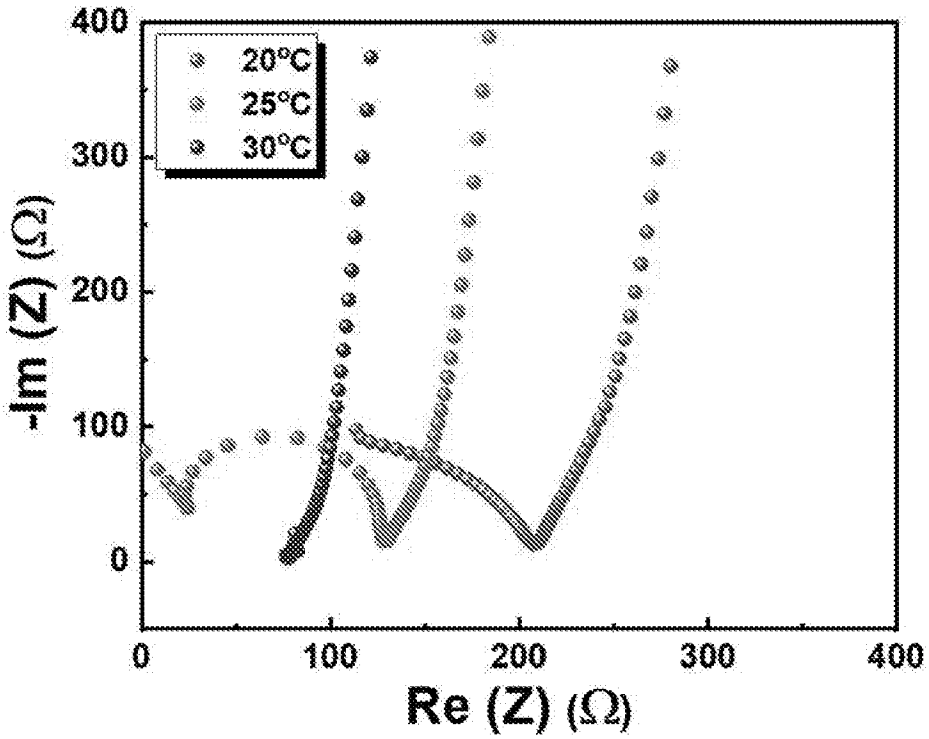

FIGURE 12

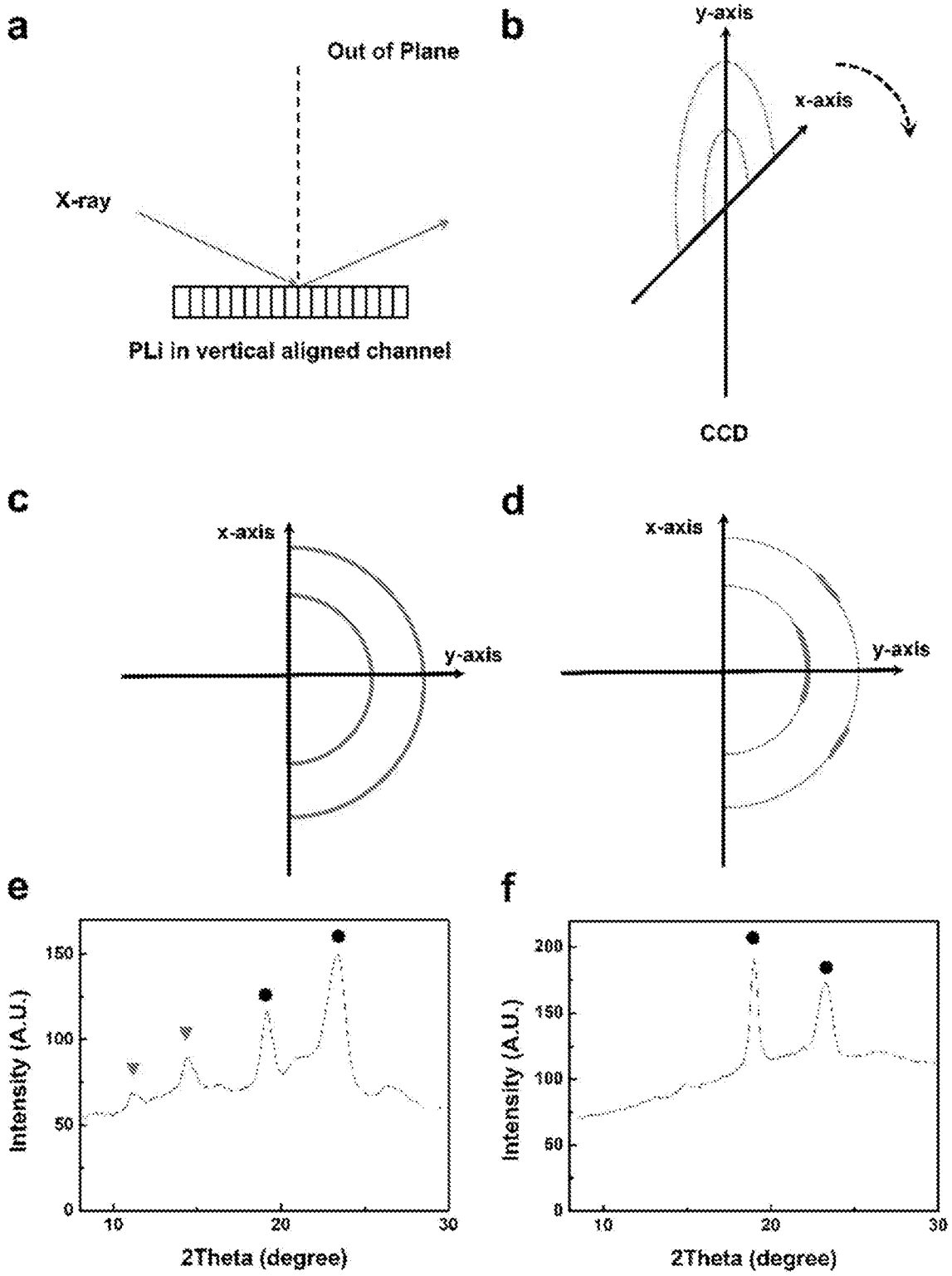
a
Out of Plane
X-ray
PLi in vertical aligned channel
b
y-axis
x-axis
CCD
c
x-axis
y-axis
d
x-axis
y-axis
e
Intensity (A.U.)
2Theta (degree)
f
Intensity (A.U.)
2Theta (degree)

FIGURE 13

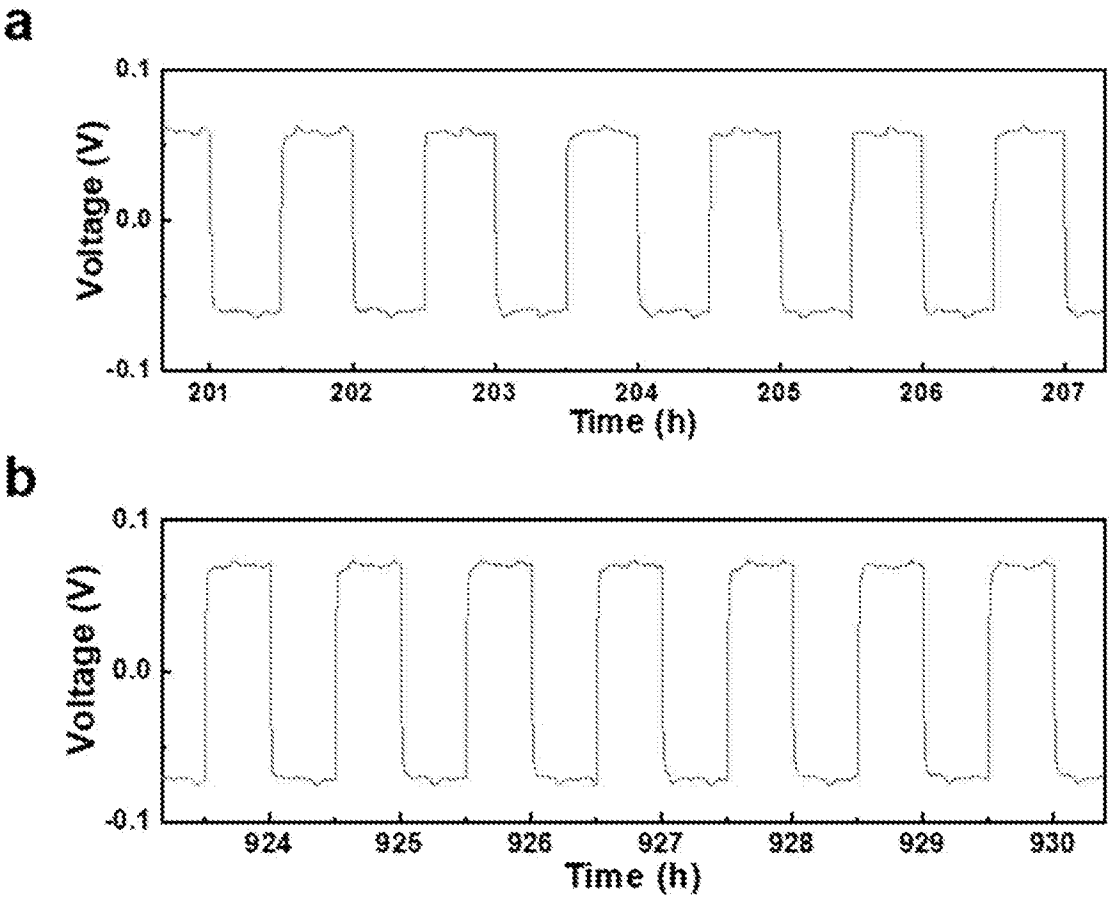
a
0.1
0.0
-0.1
Voltage (V)
201
202
203
204
205
206
207
Time (h)
b
0.1
0.0
-0.1
Voltage (V)
924
925
926
927
928
929
930
Time (h)

FIGURE 14

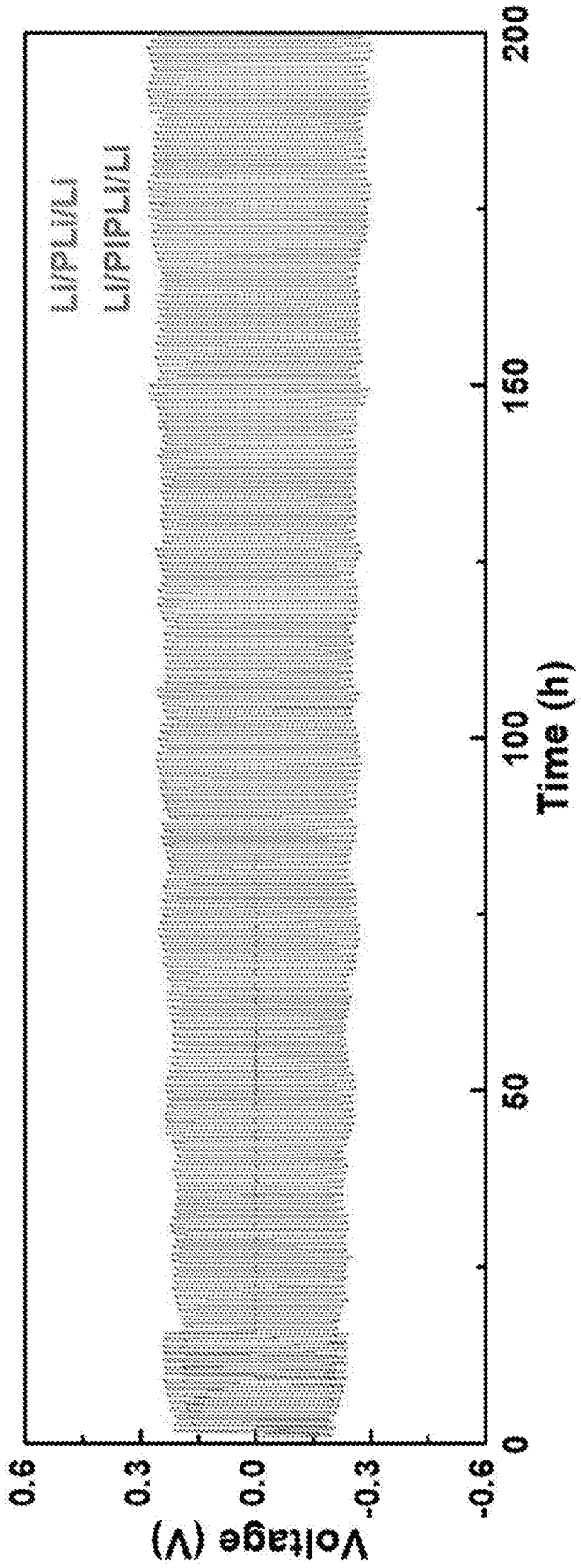
LI/PLI/LI
LI/IPLI/LI
Voltage (V)
0.6
0.3
0.0
-0.3
-0.6
0
50
100
150
200
Time (h)

FIGURE 15

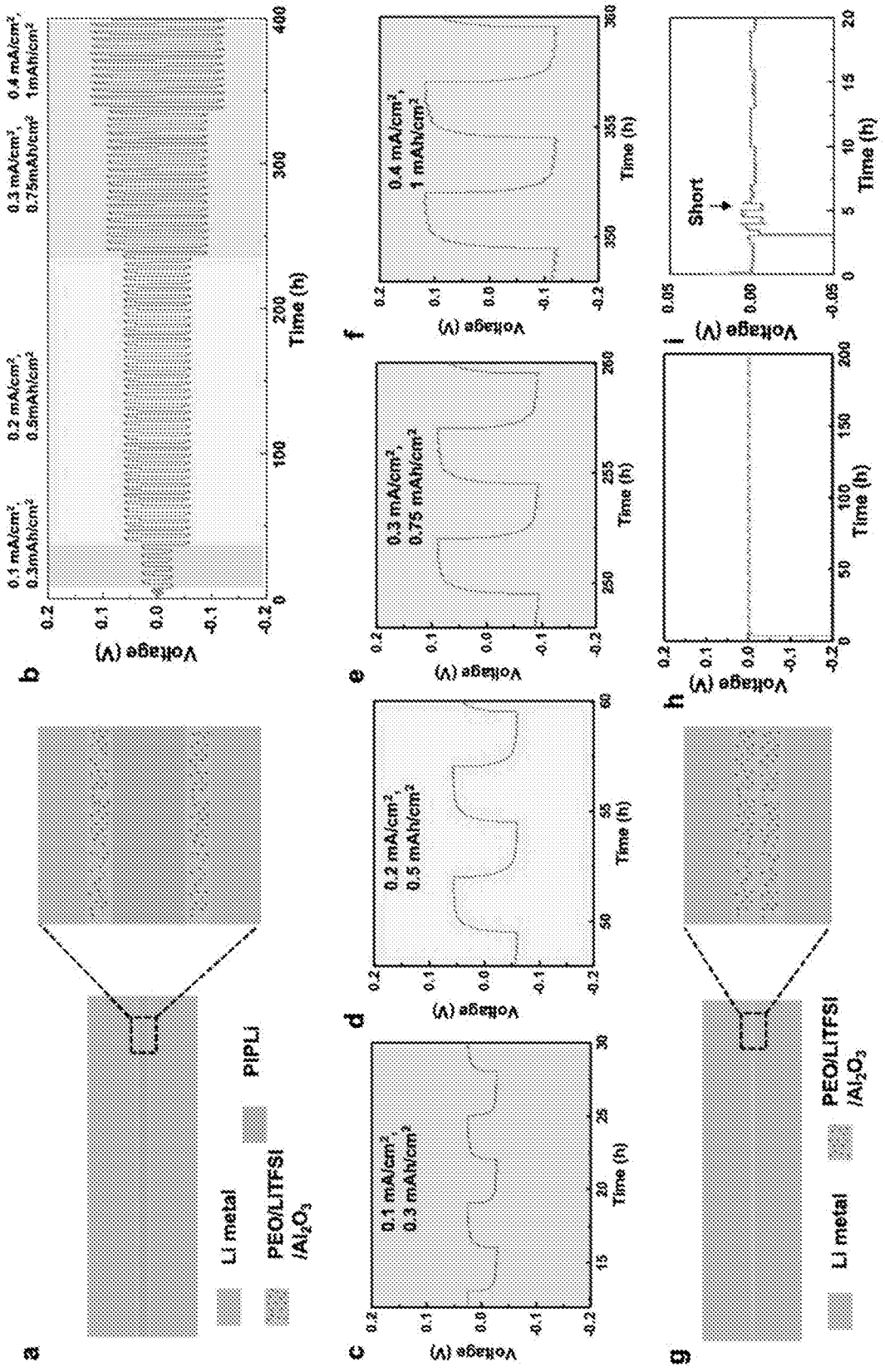
a
Li metal
PIPLi
PEO/LITFSI
/Al2O3
b
0.1 mA/cm2,
0.3mAh/cm2
0.2 mA/cm2,
0.5mAh/cm2
0.3 mA/cm2,
0.75mAh/cm2
0.4 mA/cm2,
1mAh/cm2
Voltage (V)
Time (h)
c
0.1 mA/cm2,
0.3 mAh/cm2
d
0.2 mA/cm2,
0.5 mAh/cm2
e
0.3 mA/cm2,
0.75 mAh/cm2
f
0.4 mA/cm2,
1 mAh/cm2
g
Li metal
PEO/LITFSI
/Al2O3
h
i
Short

FIGURE 16

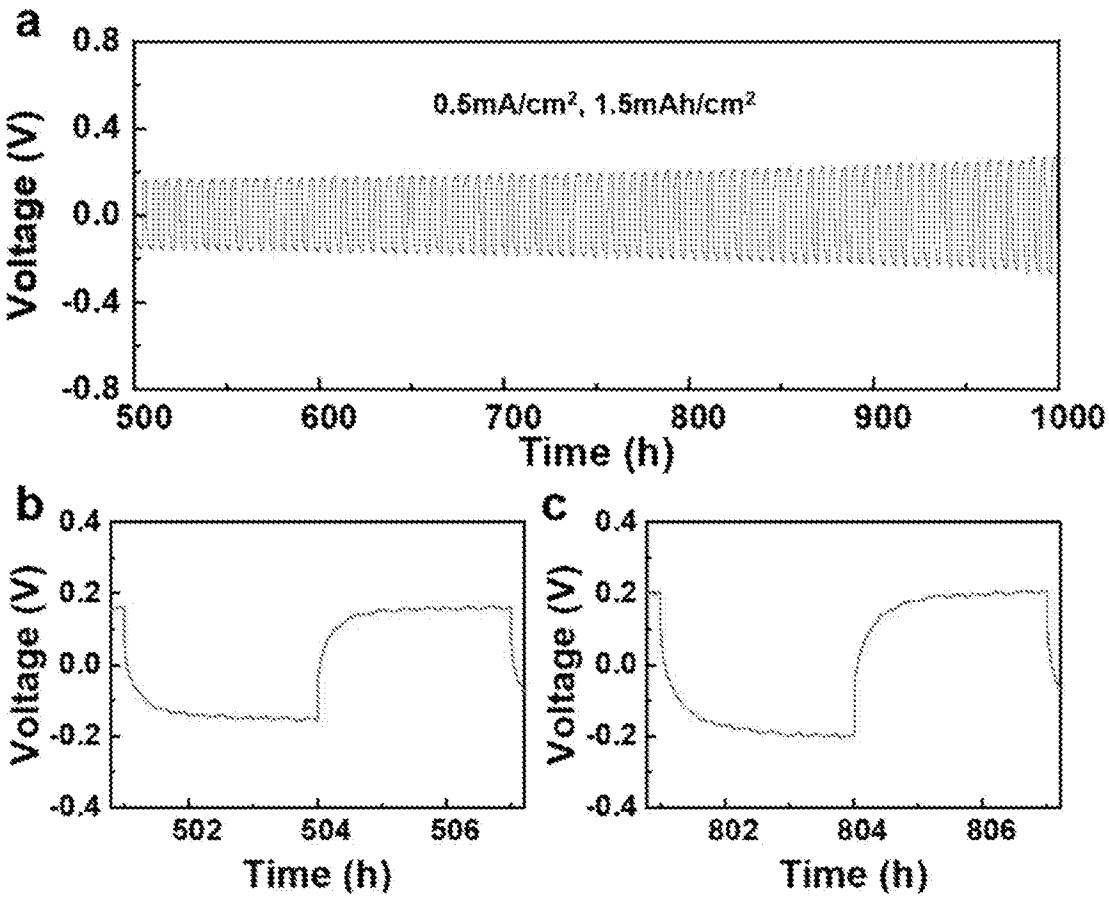

FIGURE 17

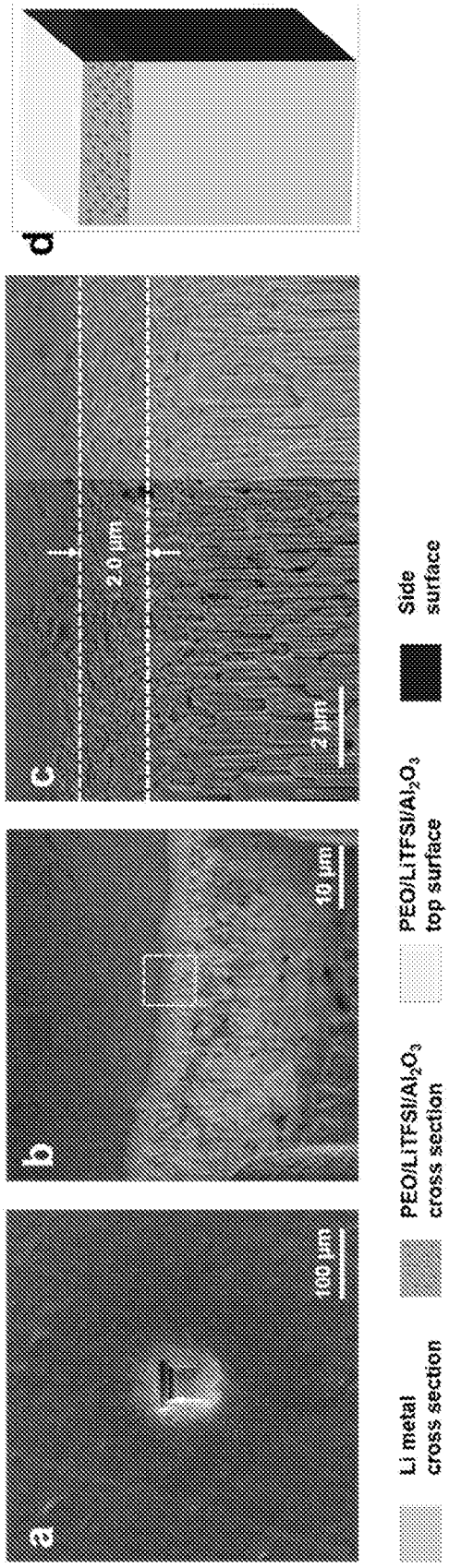
a
100 µm
b
10 µm
c
20 µm
2 µm
d
Li metal cross section
PEO/LiTFSI/Al2O3 cross section
PEO/LiTFSI/Al2O3 top surface
Side surface

FIGURE 18

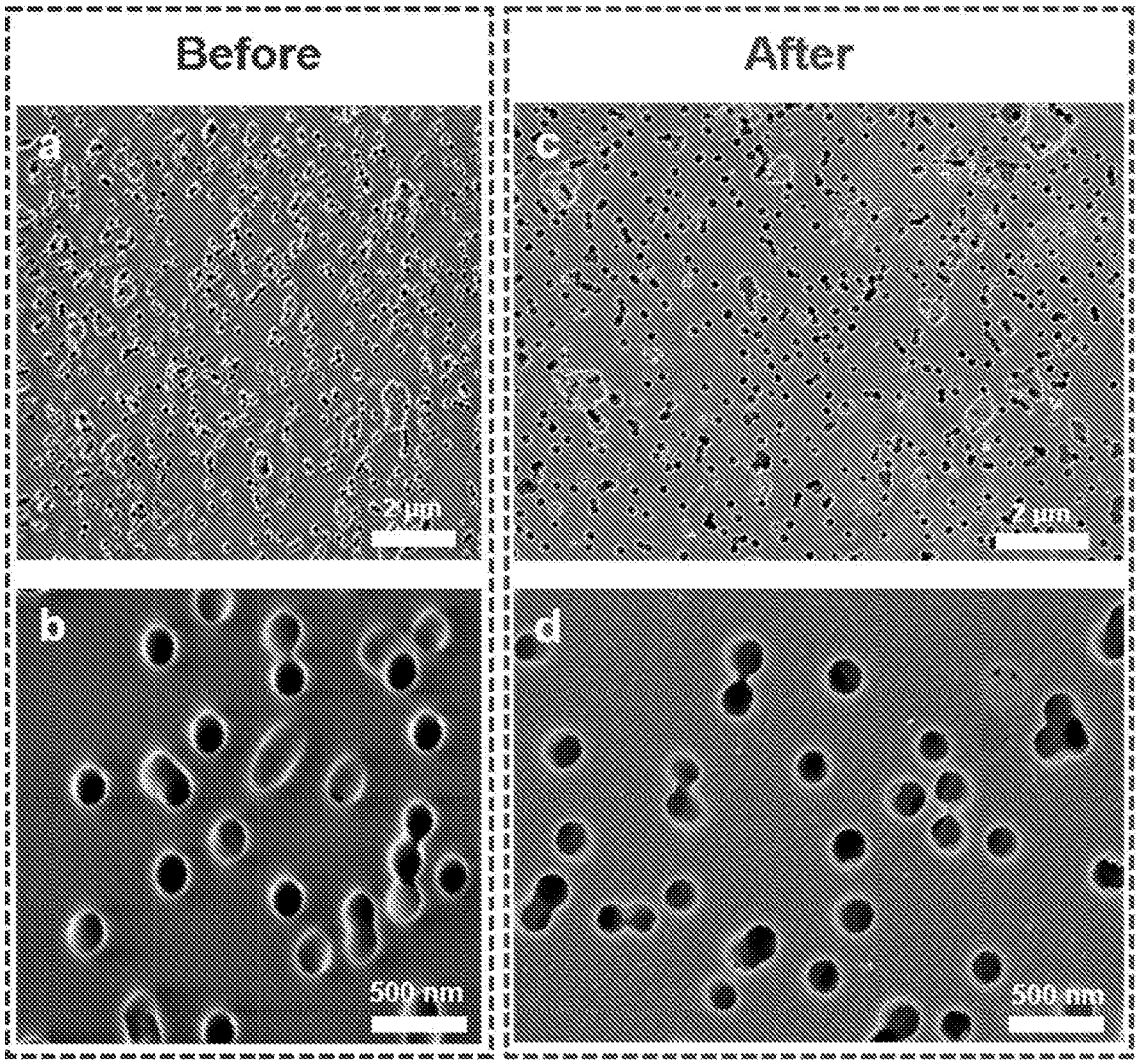

FIGURE 19

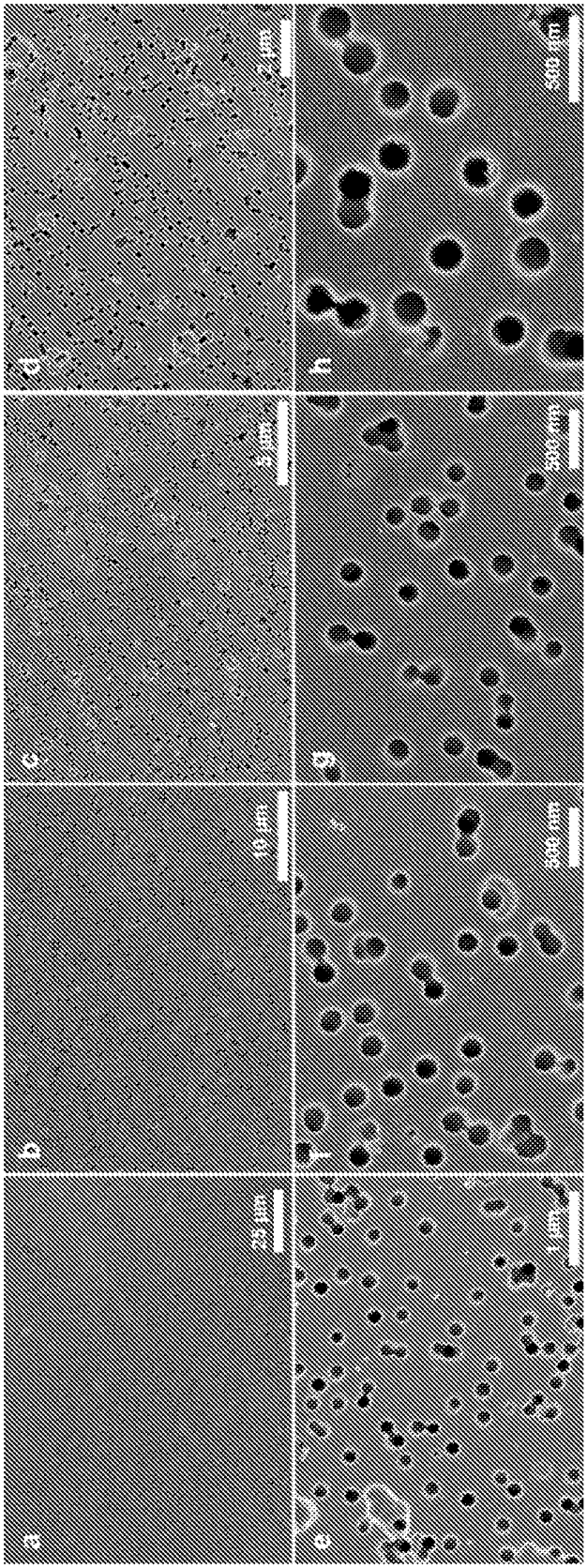

FIGURE 20

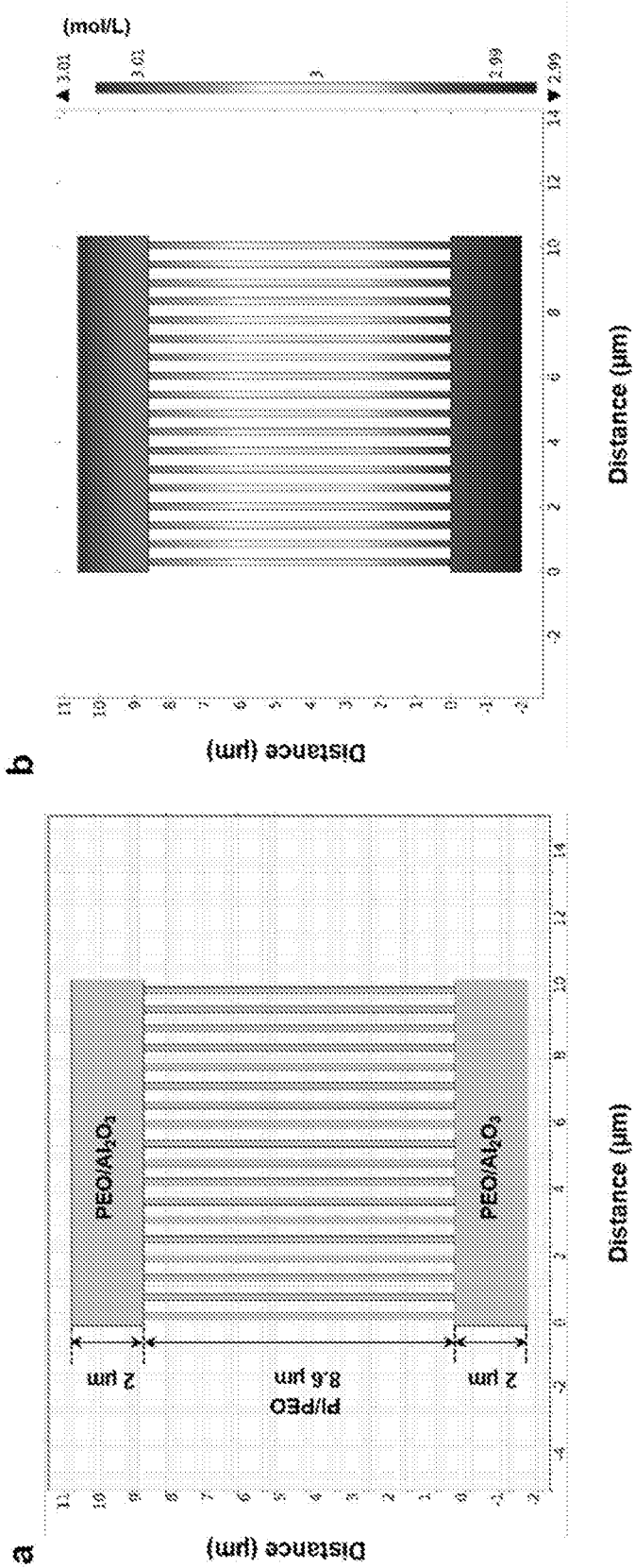
(mol/L)
3.01
3
2.99
Distance (μm)
b
PEO/Al2O3
PEO/Al2O3
2 μm
8.6 μm
PI/PEO
2 μm
Distance (μm)
a

FIGURE 21

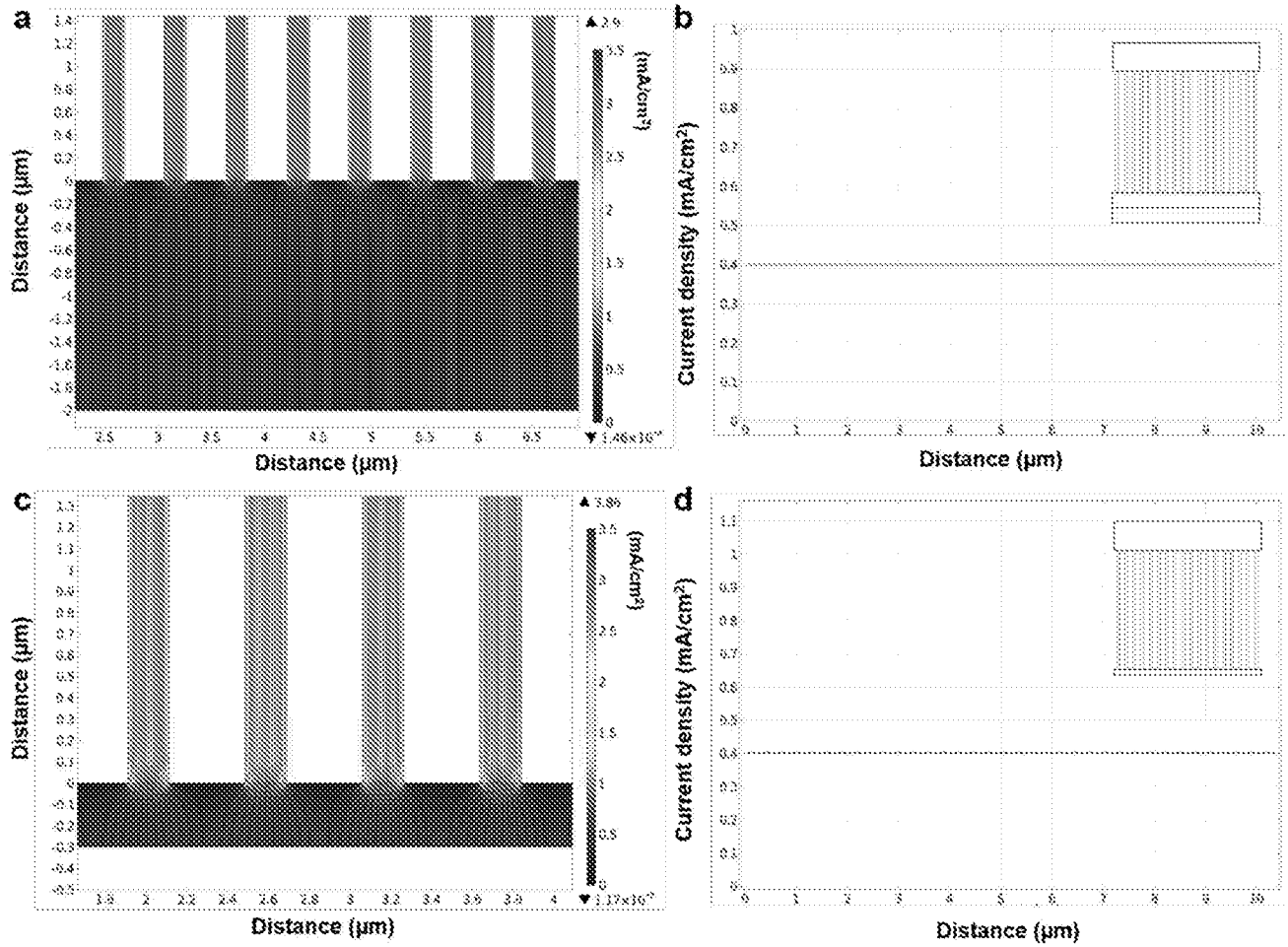
a
Distance (μm)
Distance (μm)
(mA/cm²)
b
Current density (mA/cm²)
Distance (μm)
c
Distance (μm)
Distance (μm)
(mA/cm²)
d
Current density (mA/cm²)
Distance (μm)

FIGURE 22

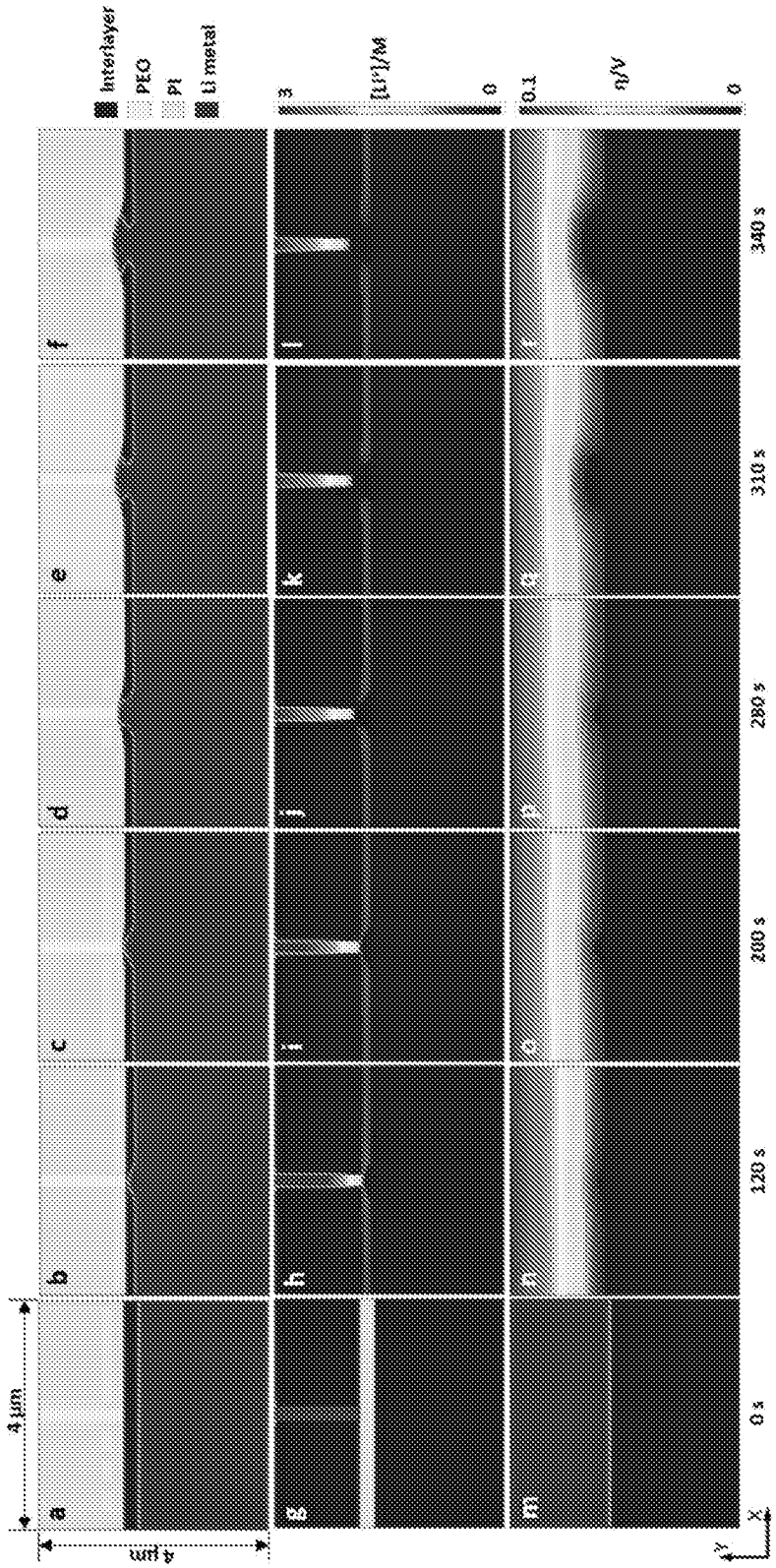
Interlayer
PEO
Pt
Li metal
3
[Li+]/M
0
0.1
η/V
0
4 μm
4 μm
a
b
c
d
e
f
g
h
i
j
k
l
m
n
o
p
q
r
0 s
120 s
200 s
280 s
310 s
340 s
x
y

FIGURE 23

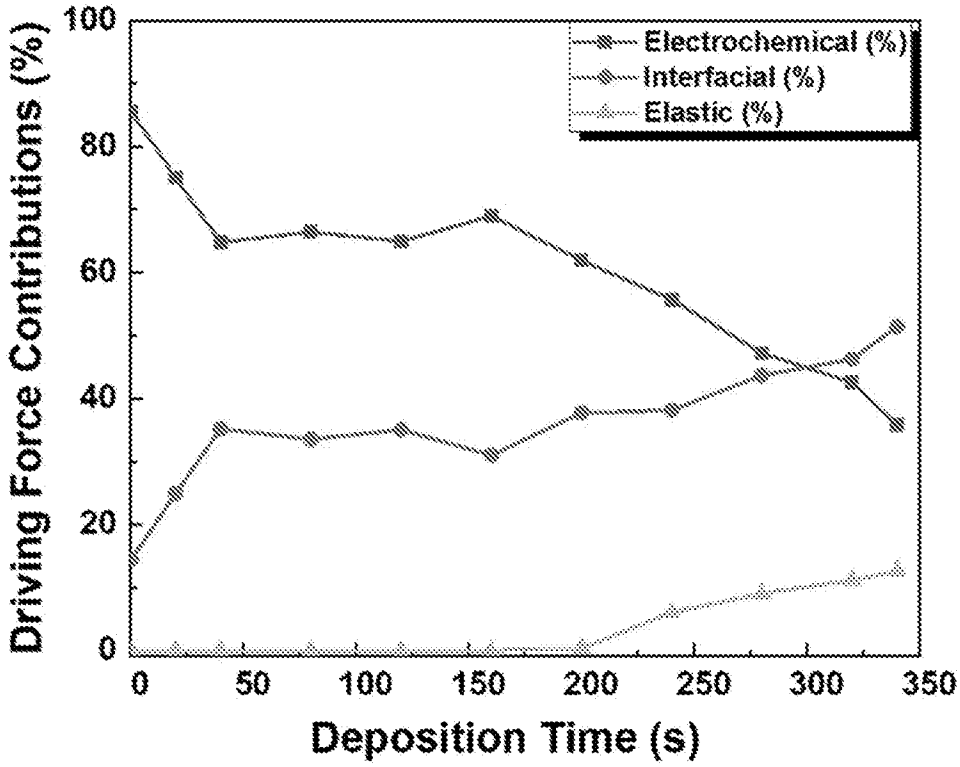
Electrochemical (%)
Interfacial (%)
Elastic (%)
Driving Force Contributions (%)
0
20
40
60
80
100
0
50
100
150
200
250
300
350
Deposition Time (s)

FIGURE 24

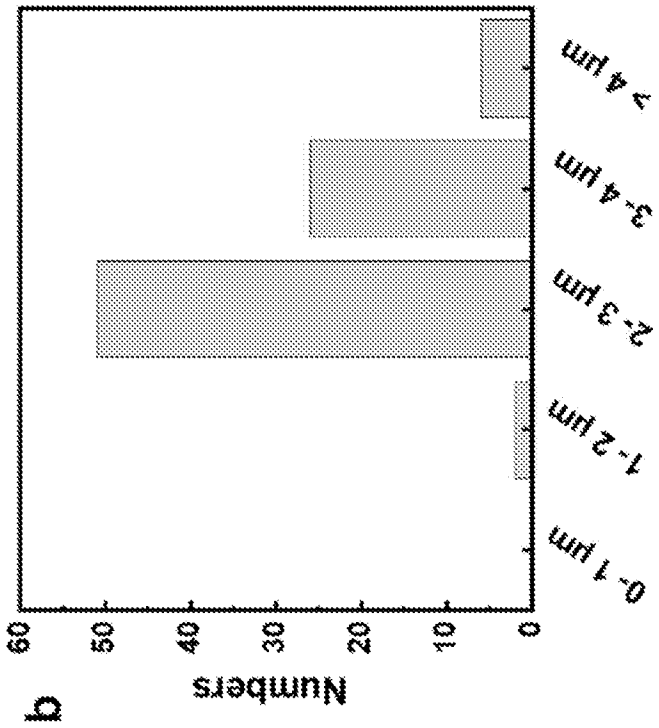

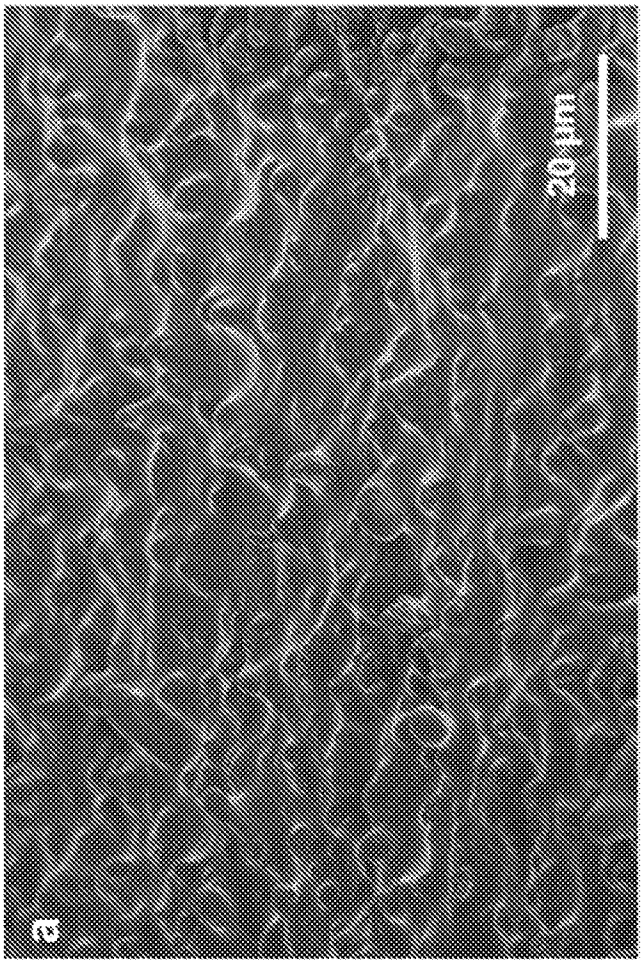

FIGURE 25

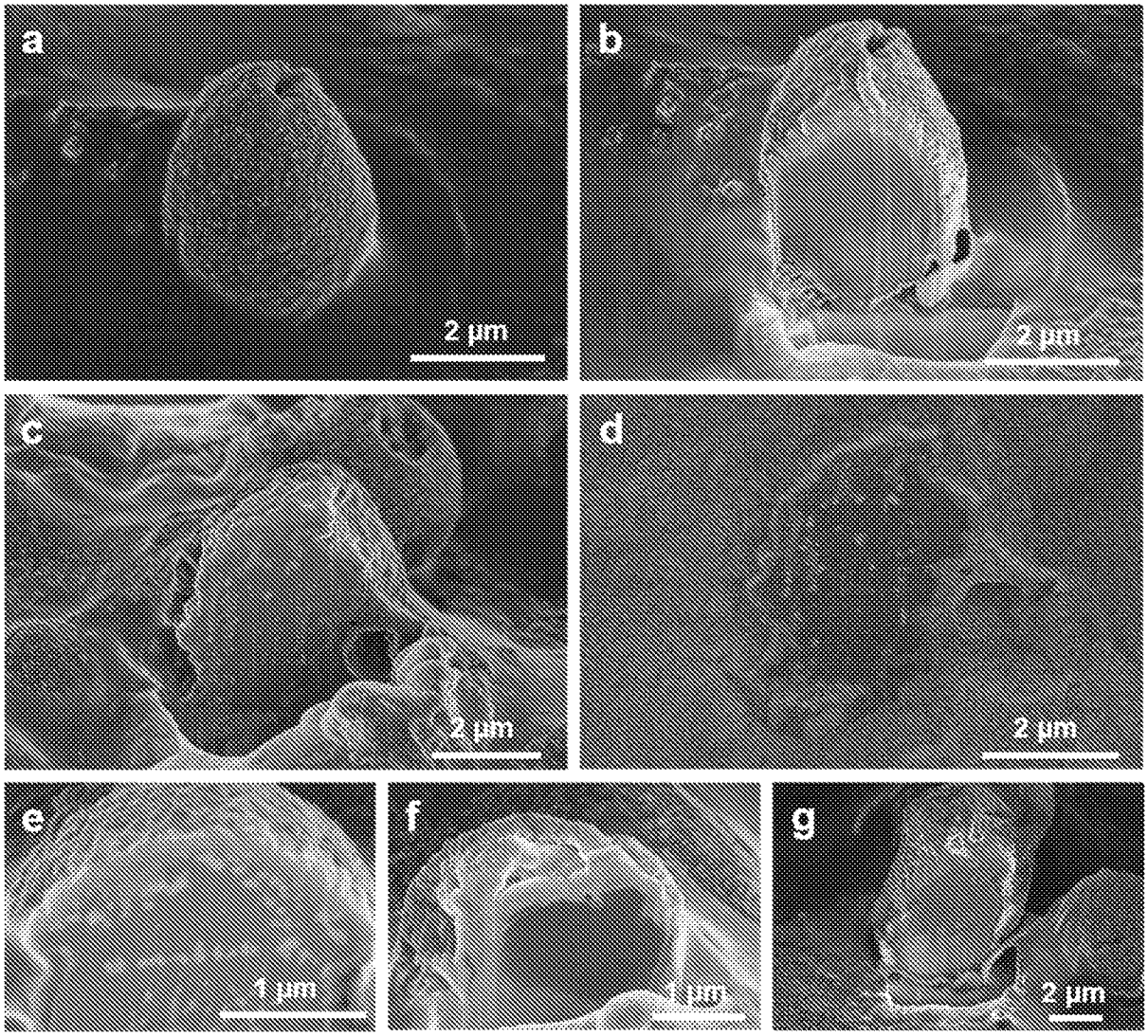

FIGURE 26

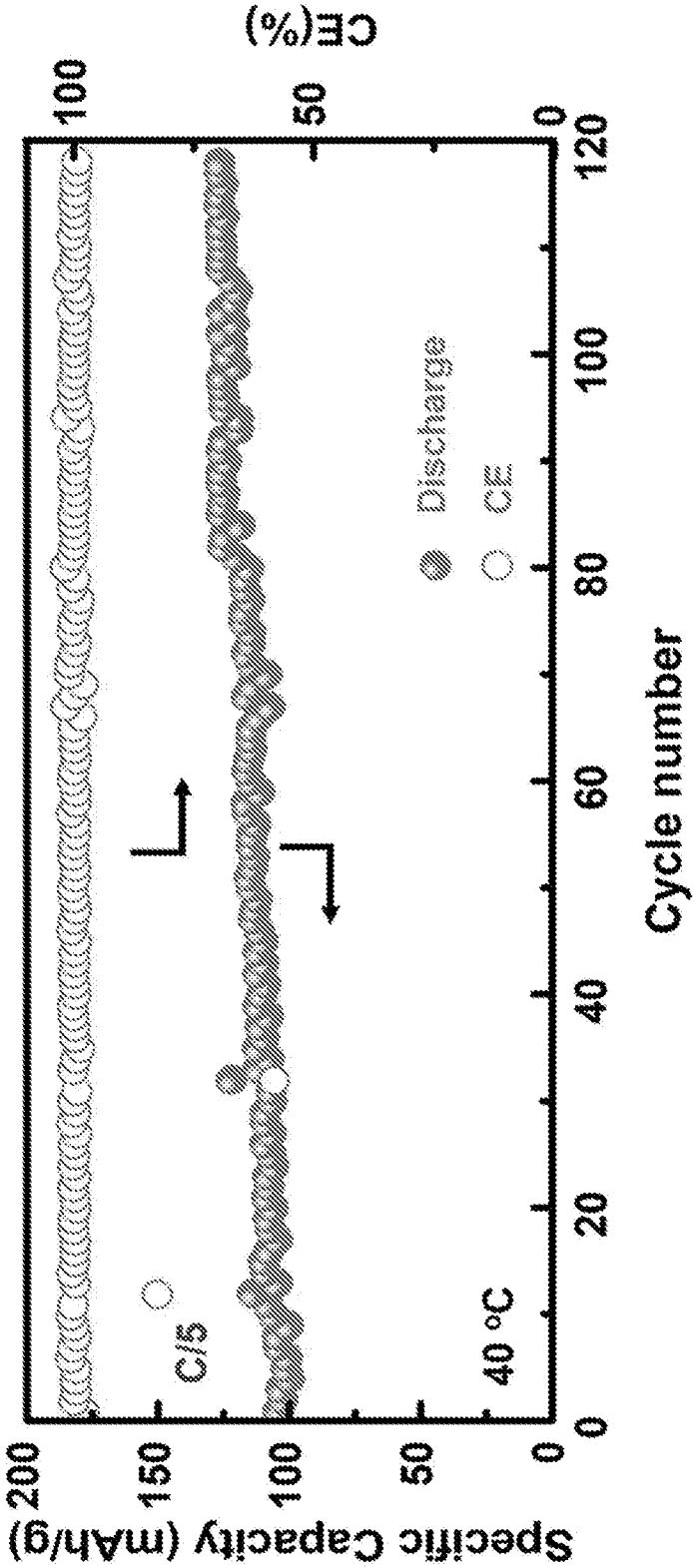
CE(%)
100
50
0
120
100
80
60
40
20
0
Cycle number
Discharge
CE
C/5
40 °C
200
150
100
50
0
Specific Capacity (mAh/g)

FIGURE 27

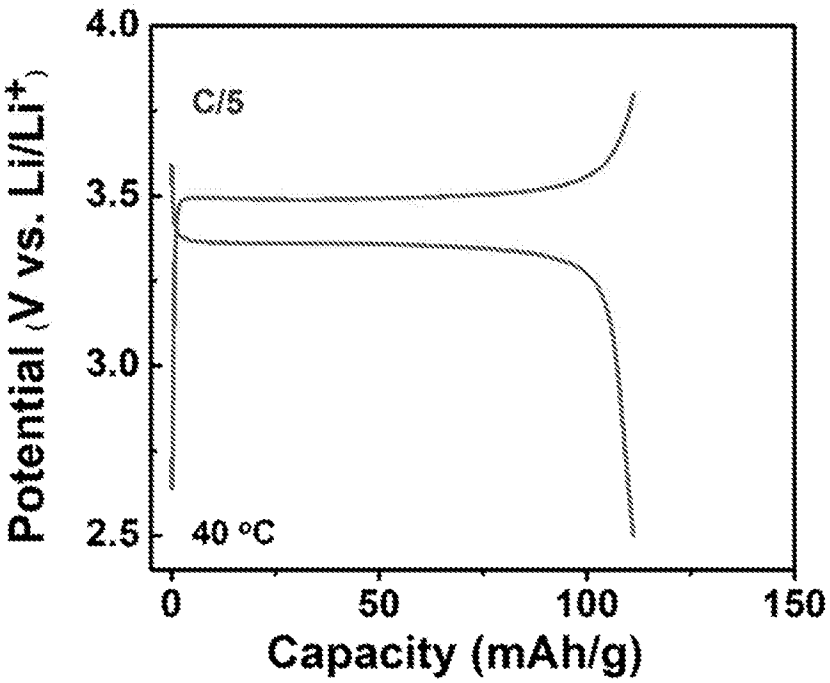
4.0
3.5
3.0
2.5
C/5
40 °C
0
50
100
150
Capacity (mAh/g)
Potential (V vs. Li/Li+)

FIGURE 28

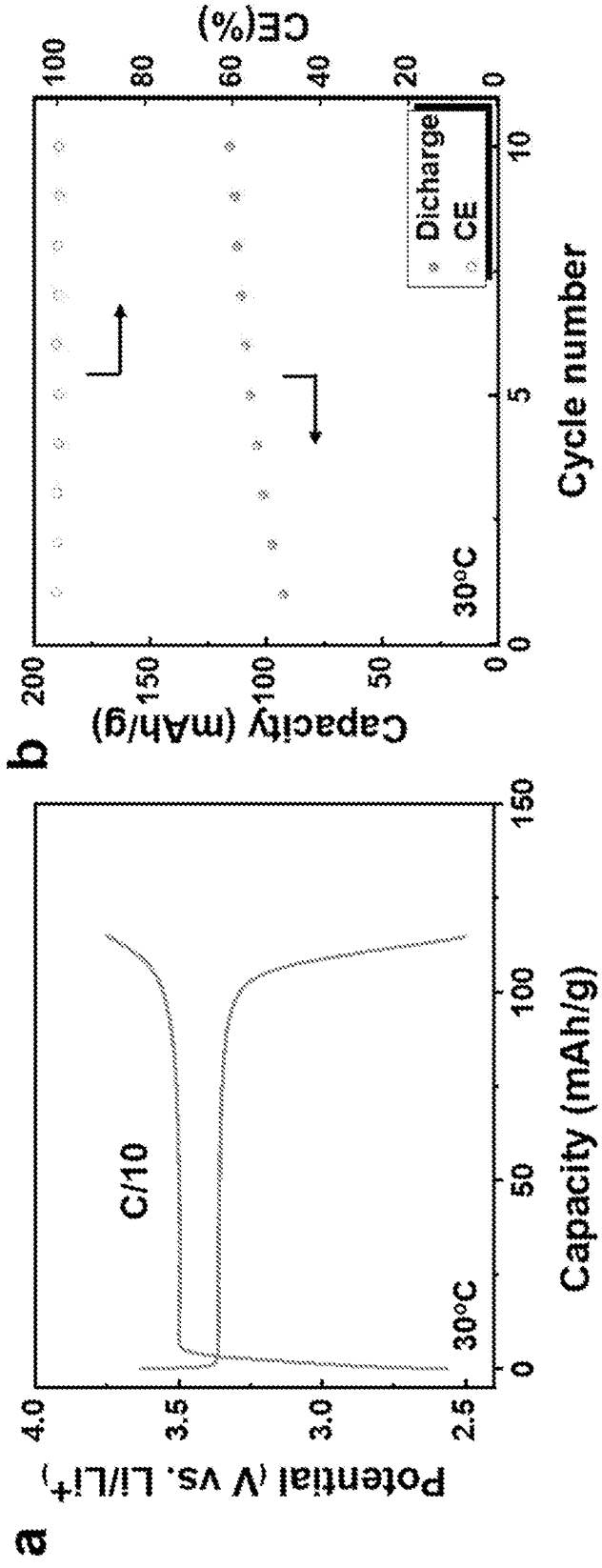
a
Potential (V vs. Li/Li+)
4.0
3.5
3.0
2.5
C/10
30°C
0
50
100
150
Capacity (mAh/g)
b
Capacity (mAh/g)
200
150
100
50
0
CE(%)
100
80
60
40
20
0
Discharge
CE
30°C
0
5
10
Cycle number

FIGURE 29

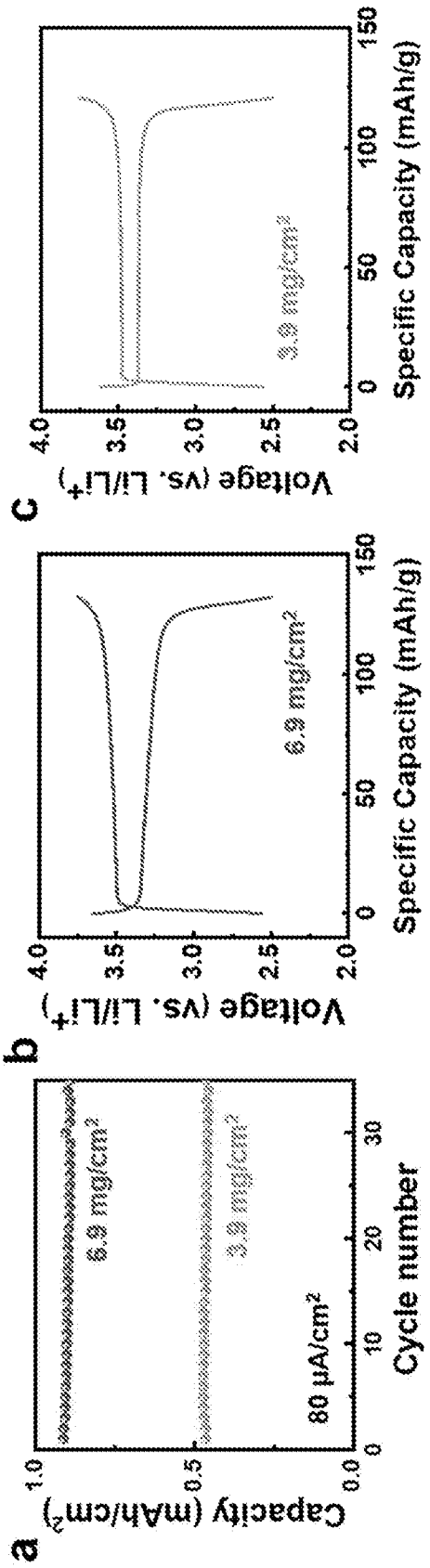
a
Capacity (mAh/cm²)
1.0
0.5
0.0
0
10
20
30
Cycle number
6.9 mg/cm²
3.9 mg/cm²
80 μA/cm²
b
Voltage (vs. Li/Li⁺)
4.0
3.5
3.0
2.5
2.0
0
50
100
150
Specific Capacity (mAh/g)
6.9 mg/cm²
c
Voltage (vs. Li/Li⁺)
4.0
3.5
3.0
2.5
2.0
0
50
100
150
Specific Capacity (mAh/g)
3.9 mg/cm²

INTERNATIONAL SEARCH REPORT

International application No.
PCT/US2020/026737

A. CLASSIFICATION OF SUBJECT MATTER

H01M 10/0565(2010.01)i, H01M 10/052(2010.01)i

According to International Patent Classification (IPC) or to both national classification and IPC

B. FIELDS SEARCHED

Minimum documentation searched (classification system followed by classification symbols)
H01M 10/0565; C08J 5/22; C08J 9/28; C08J 9/40; H01M 10/0525; H01M 10/0562; H01M 10/058; H01M 10/36; H01M 4/02; H01M 8/10

Documentation searched other than minimum documentation to the extent that such documents are included in the fields searched
Korean utility models and applications for utility models
Japanese utility models and applications for utility models

Electronic data base consulted during the international search (name of data base and, where practicable, search terms used)
eKOMPASS(KIPO internal) & Keywords: solid electrolyte, porous matrix, filler, channel

C. DOCUMENTS CONSIDERED TO BE RELEVANT

Category*	Citation of document, with indication, where appropriate, of the relevant passages	Relevant to claim No.
X	JP 4365098 B2 (SHARP KABUSHIKI KAISHA) 18 November 2009 claims 1, 7; paragraphs [0032]-[0036]	1-3,8-15
Y		4-7
Y	KR 10-1499731 B1 (KWANGJU INSTITUTE OF SCIENCE AND TECHNOLOGY) 09 March 2015 claim 1; paragraph [0033]; figures 1b, 2a	4-7
X	CN 103265721 A (HUAZHONG UNIVERSITY OF SCIENCE & TECHNOLOGY) 28 August 2013 abstract; claims 1, 2, 7	1-3,8-15
X	CN 105161761 A (SHANDONG YUHUANG NEW ENERGY TECHNOLOGY CO., LTD. et al.) 16 December 2015 abstract; claims 1-10	1-3,8-15
A	CN 106654363 B (UNIVERSITY OF SCIENCE & TECHNOLOGY BEIJING) 10 May 2017 the entire document	1-15

☐ Further documents are listed in the continuation of Box C.

☒ See patent family annex.

* Special categories of cited documents:
"A" document defining the general state of the art which is not considered to be of particular relevance
"D" document cited by the applicant in the international application
"E" earlier application or patent but published on or after the international filing date
"L" document which may throw doubts on priority claim(s) or which is cited to establish the publication date of another citation or other special reason (as specified)
"O" document referring to an oral disclosure, use, exhibition or other means
"P" document published prior to the international filing date but later than the priority date claimed
"T" later document published after the international filing date or priority date and not in conflict with the application but cited to understand the principle or theory underlying the invention
"X" document of particular relevance; the claimed invention cannot be considered novel or cannot be considered to involve an inventive step when the document is taken alone
"Y" document of particular relevance; the claimed invention cannot be considered to involve an inventive step when the document is combined with one or more other such documents,such combination being obvious to a person skilled in the art
"&" document member of the same patent family

Date of the actual completion of the international search	Date of mailing of the international search report
17 July 2020 (17.07.2020)	**17 July 2020 (17.07.2020)**

Name and mailing address of the ISA/KR
International Application Division
Korean Intellectual Property Office
189 Cheongsa-ro, Seo-gu, Daejeon, 35208, Republic of Korea
Facsimile No. +82-42-481-8578

Authorized officer
MIN, In Gyou
Telephone No. +82-42-481-3326

INTERNATIONAL SEARCH REPORT

Information on patent family members

International application No.

PCT/US2020/026737

Patent document cited in search report	Publication date	Patent family member(s)	Publication date
JP 4365098 B2	18/11/2009	CN 1528028 A TW 554560 B WO 02-078114 A1	08/09/2004 21/09/2003 03/10/2002
KR 10-1499731 B1	09/03/2015	KR 10-2010-0058243 A	03/06/2010
CN 103265721 A	28/08/2013	CN 103265721 B	31/12/2014
CN 105161761 A	16/12/2015	None	
CN 106654363 B	26/02/2019	CN 106654363 A	10/05/2017